3D Volume Ultrasound:
Probe Calibration and Extended Field-of-View

by

Tony Chingtoa Poon

B.A.Sc., University of British Columbia, Canada, 2003

A THESIS SUBMITTED IN PARTIAL FULFILLMENT OF
THE REQUIREMENTS FOR THE DEGREE OF

MASTER OF APPLIED SCIENCE

in

THE FACULTY OF GRADUATE STUDIES

(Electrical and Computer Engineering)

THE UNIVERSITY OF BRITISH COLUMBIA

August 2005

Abstract

Real-time 3D ultrasound is a new generation ultrasound system that uses a dedicated hand-held probe to create volume data sets instead of standard 2D cross-sectional images. For applications in image-guided surgery and radiation therapy, a position tracker is added to the probe so that the volumes can be located in space. Calibration plays a critical role in determining the overall accuracy of an ultrasound volume tracking system. In this thesis, three calibration methods are developed specifically for 3D probes. The three methods are based on a IXI-wire phantom, a cube phantom and a stylus. The performance of each method is evaluated in terms of calibration reproducibility, point accuracy and reconstruction accuracy by distance measurement. The mean errors in the reproducibility tests are 1.50 mm (IXI-wire), 1.16 mm (cube) and 5.13 mm (stylus). The RMS errors of the point accuracy measure are 2.15 mm (IXI-wire), 4.91 mm (cube) and 2.36 mm (stylus). The RMS errors of the reconstruction accuracy by distance measure are 1.52 mm (IXI-wire), 1.59 mm (cube) and 1.85 mm (stylus). Overall, the IXI-wire phantom achieved the best results among the three.

3D extended field-of-view ultrasound creates panoramic views from a set of volume acquired from a dedicated 3D ultrasound machine and a position tracker. A simple compounding technique can then be used to combine the volumes together using only the position measurements but some misalignment remains. We applied two different registration methods to correct these errors in the overlapping regions. The first method divides the overlap into smaller blocks and warps the blocks to best align the features. The second method uses rigid body registration of the blocks. Experiments *in vitro* and *in vivo* showed that block-based registration with warping produced the most reproducible results and the greatest increase in similarity among the overlapping regions. It also produced the best reconstruction accuracy with a mean distance measurement error of 0.4 mm on a fetus phantom.

Table of Contents

List of Tables

List of Figures

Glossary

Artifacts	Any incorrect features that are shown on the image to represent an anatomical structure.
Axial	Depth direction of an image (along columns of pixels).
B-scan	Brightness scan to represent the ultrasound echo on display.
Calibration	To calculate the offset from the position tracker mounted on the probe handle to the ultrasound volume.
Correlation coefficient	A measure of similarity between two images or volumes.
CT	Computed Tomography.
Elevational	Perpendicular to an image.
Field-of-view	The extents of view captured by the ultrasound probe.
Freehand	The movement of an ultrasound probe by hand without any spatial restrictions.
In vitro	Within an artificial environment.
In vivo	Within the living body.
Intraoperative	Performed during the operation of a surgery.
IRLED	Infrared light emitting diode.
Isosurface	A set of voxels with the same intensity value comprise a surface.
Lateral	Width direction of an image (along rows of pixels).
MRI	Magnetic Resonance Imaging.
Multiplanar re-slice	A 2D image corresponding to a user-defined cut-plane through the volume for visualizing the spatial relationship among structures.
Neurosurgery	Surgery concerned with the treatment of diseases and disorders of the brain, spinal cord and the nervous system.
Orientation	The three degrees of freedom (roll, pitch, yaw) that determine the direction of the volume coordinate system.
Phantom	An artificial object with known geometrical characteristic that is used for probe calibration and testing.
Position	The coordinate of a point in a Cartesian coordinate system. The three

	degree of freedom (x, y, z) that determines the origin of the volume coordinate system.
Probe	The transducer that transmits ultrasound pulses and that receives the associated echoes.
Reconstruction	The stage of the extended field-of-view system where individual volumes are combined into a common space.
Registration	Calculation of position and orientation that matches features between two sets of data.
Reverberation	Multiple ultrasound reflections between a structure and the probe.
Spatial compounding	The averaging of multiple overlapping data for the purpose of reducing speckle.
Speckle	Acoustic noise in ultrasound imaging due to the coherent nature of ultrasound.
Visualization	Visual depiction of the ultrasound data, normally used by doctors to make an accurate diagnosis of the patient's condition and to assess the patient's response to therapy.
Volume	A 3D array of regularly-spaced voxels.
Volume rendering	To reconstruct a continuous function to describe the volume data set and to project it onto a 2D viewing plane from a desired point of view.
Voxel	Volume elements that contain intensity information.
Warping	The non-rigid displacements of voxels according to a set of control points.

Acknowledgements

I would like to gratefully acknowledge my supervisor, Dr. Robert Rohling, who has been a rich source of inspiration and support for my thesis project. His guidance and constructive feedback have been important to the successful development of my research. His expertise in the area of ultrasound imaging was a key part to the innovation of my work.

I would like to thank my love, Karina Lau, for her continuous encouragement during the course of my research. She contributed to my work in extended field-of-view by operating the acquisition system which takes ultrasound volumes across my body for *in vivo* experiments. My family should be thanked too, for their support throughout my years of education, especially my mother who impressed me of the value of education.

I would also like to thank my friends at UBC, especially those in the Robotic and Control Laboratory, for their valuable time for our discussions and chitchats. The help from the technicians in the electrical engineering machine shop for the construction of phantoms and apparatuses is also greatly appreciated.

Finally, I would like to acknowledge the research assistantship granted by Dr. Rohling, from the BC Advanced Systems Institute and the Natural Science and Engineering Research Council, for supporting me in completing my Masters.

Publications

A journal article based on Chapter 2 has been accepted for publication:
Poon TC, Rohling RN. Comparison of calibration methods for spatial tracking of a 3D ultrasound probe. Ultrasound in Medicine and Biology, 2005; 31(8): 1095-1108.

A journal article based on Chapter 3 has been submitted for publication:
Poon TC, Rohling RN. Three dimensional extended field-of-view ultrasound. Ultrasound in Medicine and Biology, 2005 (submitted).

Chapter 1 Introduction

Ultrasound imaging is a noninvasive method that reveals important diagnostic information from patients. Different from other medical imaging modalities (such as X-ray, CT and MRI), ultrasound rapidly and conveniently creates images from a hand-held probe. The operator holds the probe in contact with the patient's body and the ultrasound scanner produces real-time images of the anatomical structure within the cross-sectional plane of the probe. The probe excites pulses of ultrasound energy that propagate through the patient's body; the same probe also receives echoes of the energy from the anatomical structures. In response to these echoes, the probe produces electronic signals back to the scanner for the reconstruction of an ultrasound image. The generation of the image is based on the principle that the depth of various anatomical structures can be computed by multiplying the propagation speed of the pulse and the elapsed time of the echoes. Brightness of the image corresponds to the strength of the echo. This is called the pulse-echo principle that is the cornerstone of the ultrasound imaging technology.

Advances in image quality and visualization clarity have gained growing acceptance by physicians who decide on an imaging modality for diagnostics. The proportion of ultrasound among all medical imaging studies is increasing; in recent years, one out of every four studies is now performed with ultrasound (WFUMB, 1997). The drawback of ultrasound imaging is that it does not work well in the presence of bone or gas because the ultrasound energy is almost completely reflected, preventing further penetration (Wells, 1999). Otherwise, ultrasound can depict nearly all soft-tissue organs.

1.1 The Need for Probe Calibration

In some ultrasound guided procedures, it is necessary to measure the position and orientation of the ultrasound probe in space. Examples of ultrasound probe tracking applications include guidance in neurosurgery (Comeau et al. 2000) and image-guided radiation therapy (Bouchet, et al. 2001). In neurosurgery, intraoperative ultrasound images of the brain are aligned with preoperative magnetic resonance (MR) images in

order to determine the amount of tissue shift that has occurred during the procedure. In radiation therapy, the images are measured with respect to the treatment equipment, so that the anatomical target can be aligned with previously acquired computed tomography (CT) images and its corresponding radiation dose plan.

To measure the position and orientation of each cross-sectional image (also called a B-scan), an external tracking system is used. The tracking system indirectly measures the positions of the ultrasound images by measuring one or more sensors attached to the probe handle. The most common tracking systems use either electromagnetic or optical sensing technology, where a sensor (marker or receiver) is mounted on the probe and a base unit (camera or transmitter) is placed on a nearby table, wall or ceiling. Calibration of the sensors' positions on the probe handle is required. In particular, calibration determines the transformation between the coordinate systems of the sensor and the ultrasound images. Calibration plays a critical role in determining the overall accuracy of a tracked 2D ultrasound system (Prager, et al. 1998).

2D ultrasound can be extended to 3D by reconstructing a 3D volume of data from a number of 2D cross-sections. One way to create 3D volumes is to move a standard 2D probe slowly over a region in the elevation direction while capturing the cross-sectional images. A volume is created from the set of 2D images, analogous to stacking a deck of cards. This is called 3D freehand ultrasound and a position sensor is often used to record the location of each cross-sectional image. If the reconstructed volume is only used for visualization and localized measurement purposes (such as volume rendering and head-circumference measurements), then the tracking system simply needs to measure the relative position and orientation of individual images. For the image-guided procedures, such as neurosurgery and radiation therapy, the 3D volume of ultrasound data must be measured with respect to the fixed global coordinate system associated with other equipment (e.g. a surgical table) so that the absolute spatial location of the anatomical target is measured.

1.1.1 Motivations

A new generation of 3D ultrasound machines is now available commercially in which a handheld 3D probe is dedicated to produce volumetric ultrasound data, instead of 2D images. The volume is reconstructed using a special mechanism inside the probe to sweep the images in rapid succession through a volume-of-interest (Figure 1-1). The main advantage of a 3D probe is the ability to acquire volumes of the examination area in real-time. The disadvantages are that the 3D probe is heavier, bulkier and more expensive than a 2D probe. In clinical practice, the 3D probe is held steady over a volume of interest, while a freehand system requires the 2D probe to be slowly and steadily swept over the volume of interest. This means the scanning protocol is slightly different.

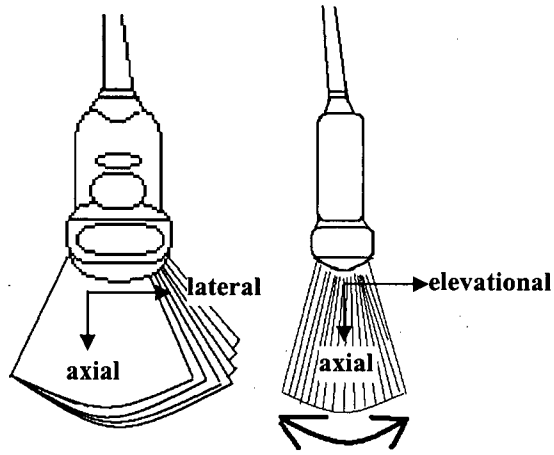

Figure 1 - 1 : A handheld 3D probe to produce volumetric ultrasound data. The volume is reconstructed by a stack of 2D images.

For some visualization and measurement applications, the dedicated 3D probe can replace the freehand acquisition 2D probe set-up to acquire 3D ultrasound volumes. But for guidance applications in radiation therapy and neurosurgery, a position sensor is still required for the absolute position measurements of the ultrasound volumes. Thus, for those applications, calibration is still required to solve the transformation between the coordinate systems of the sensors on the 3D probe and the ultrasound volumes. Calibration is therefore one of the main focal points of this thesis.

1.1.2 Literature Review

There are a number of different calibration methods reported in the literature. Two early descriptions of calibration were presented by Barbe et al. (1993) for computer assisted spine surgery and by Nelson and Elvins (1993) for visualization of 3D ultrasound. Soon after, two independent investigations focused specifically on the issue of calibration and accuracy (Detmer et al. 1994, Trobaugh et al. 1994). The number of subsequent papers on ultrasound calibration grew quickly. New methods continue to appear and differ mainly in terms of the geometrical properties of the phantoms to achieve more accurate calibration results or easier processing steps than previous methods. The majority of the methods can be classified according to four kinds of phantoms: wire, plane, stylus (precalibrated tracking pointer) and irregularly shaped phantoms. The geometrical properties of the phantoms are determined either by accurate construction of the phantom (e.g., wire phantoms), external measurements (e.g., calipers) and imaging by another modality (e.g., computed tomography). Several literature reviews of 2D probe calibration methods are available (Lindseth et al. 2003; Muratore and Galloway 2001; Mercier et al. 2004).

There are only two articles that describe calibration methods for dedicated 3D probes. Lange and Eulenstein (2002) proposed two calibration methods. The first method determines the calibration result by registering an ultrasound volume of a phantom with its associated CT volume. The phantom contains two egg-shaped objects sized 6.7 mL and 65.0 mL respectively. They placed fiducial markers on the exterior of the phantom and used a magnetic tracking stylus to find the positions of the markers in a global coordinate system. Because the markers also appear in the CT volume, identifying the positions of the markers reveals the position and orientation of the CT volume. Therefore, the registration of the ultrasound volume with the CT volume relates the ultrasound volume (V) to the global coordinates system (G) via the transformation matrix ${}^{G}\mathbf{T}_{V}$. The researchers also placed magnetic sensors on the ultrasound probe for tracking the position and orientation of the dedicated 3D probe in the global coordinate system. This tracking step produces the transformation between the probe (P) and the global coordinate system (G), ${}^{G}\mathbf{T}_{P}$. The transformation, ${}^{P}\mathbf{T}_{V}$, between the ultrasound volume (V) and the dedicated probe (P) is related to the two known transformations by the equation,

${}^{G}\mathbf{T}_{V} = {}^{G}\mathbf{T}_{P}\,{}^{P}\mathbf{T}_{V}$. That means that the calibration transformation, ${}^{P}\mathbf{T}_{V}$, can be computed by the equation ${}^{P}\mathbf{T}_{V} = ({}^{G}\mathbf{T}_{P})^{-1}\,{}^{G}\mathbf{T}_{V}$. This method reports 2.0 mm RMS errors in reconstruction accuracy by distance measurements on a set of points uniformly distributed inside the phantom.

The second method proposed by Lange and Eulenstein (2002) is called "hand-eye calibration". The idea is to register two ultrasound volumes acquired on the same phantom, so that a transformation loop is formed. The two volumes are acquired from two different directions. The spatial measurements (position and orientation) of the probe (*P*) are different, so the magnetic tracking system produces two different transformations, ${}^{G}\mathbf{T}_{P1}$ and ${}^{G}\mathbf{T}_{P2}$, with respect to the global coordinate system (*G*). The transformation between *P1* and *P2* is found from ${}^{P2}\mathbf{T}_{P1} = ({}^{G}\mathbf{T}_{P2})^{-1}\,{}^{G}\mathbf{T}_{P1}$. The registration of the two ultrasound volumes produces the transformation ${}^{V2}\mathbf{T}_{V1}$. The unknown calibration transformation between the ultrasound volume and the probe, ${}^{P}\mathbf{T}_{V}$, remains unchanged in the acquisition of the two volumes, because the magnetic sensors on the probe are fixed. Therefore, it can be solved by the equation ${}^{P2}\mathbf{T}_{P1}\,{}^{P1}\mathbf{T}_{V1} = {}^{P2}\mathbf{T}_{V2}\,{}^{V2}\mathbf{T}_{V1}$, where ${}^{P1}\mathbf{T}_{V1} = {}^{P2}\mathbf{T}_{V2}$ is the unknown ${}^{P}\mathbf{T}_{V}$. This method reports 2.2 mm RMS errors in reconstruction accuracy by distance measurements on a set of points uniformly distributed inside the phantom.

Bouchet et al. (2001) explored the N-wire method to solve the 3D probe calibration problem. This method was originally proposed by Comeau et al. (1998; 2000) and Pagoulatos et al. (1999; 2001) for 2D probe calibration. The calibration phantom contains 39 nylon wires in a tissue-equivalent anechoic medium. These wires form 13 N-shaped patterns at 13 different depths. The phantom was accurately constructed such that the geometry of the wires is known. The researchers placed sensors on the phantom box and measured the position and orientation of the box in the global coordinate system. When the ultrasound volume of the phantom is acquired, a segmentation algorithm is used to extract the voxels that depict the wires. Identifying the voxel positions of the wires in the ultrasound volume (*V*) with respect to their spatial positions in the global coordinate system (*G*) determines the transformation between them, ${}^{G}\mathbf{T}_{V}$. Since there are position sensors placed on the probe, the probe position and orientation are also measured during volume acquisition. The transformation between the probe (*P*) and the global

coordinate system (G), ${}^{G}\mathbf{T}_{P}$, is measured by the tracking system. The calibration transformation between the ultrasound volume (V) and the probe (P), ${}^{P}\mathbf{T}_{V}$, is determined by the equation ${}^{P}\mathbf{T}_{V} = ({}^{G}\mathbf{T}_{P})^{-1}\,{}^{G}\mathbf{T}_{V}$. The maximum error in the three dimensions of the volume is 0.4 mm in the elevation direction, 1.5 mm in the lateral direction and 1.1 mm in the axial direction. The 3D interpretation of these errors is 1.9 mm.*

The purpose of this study is to propose three calibration methods for dedicated 3D probes: IXI-wire method, stylus method (precalibrated tracking pointer) and cube method. The development of these methods was inspired by existing phantoms presented in the literature for 2D and 3D probe calibration. The IXI-wire method uses a phantom analogous to the N-wire phantom (Pagoulatos et al. 2001 and Comeau et al. 2000). The cube method is analogous to the single plane method (Prager et al. 1998), yet a 3D probe captures three orthonormal planes. The stylus method is fundamentally the same method as that used for 2D probe calibration (Muratore and Galloway. 2001). The single-point phantom used by Lindseth et al. (2003) does not track the stylus but the mathematics is very similar to the stylus method. The position of a pointer bead (single-point) is measured by Lindseth in the 2D image as an input to the calibration equations. For the 3D probe, we move the stylus to various locations within the volume instead of being constrained to a plane.

1.2 Extended Field-of-View Ultrasound

Extended field-of-view (also called panoramic) ultrasound started more than 40 years ago when a static image was produced by moving a 1D probe across the examination area using a mechanical positioning arm (Donald et al. 1958; Dietrich et al. 2002). As ultrasound technology has progressed, there has always been a tradeoff between the ultrasound dimensions and the acquisition speed. The use of the position-tracked 1D probe to produce a static image (2D) is a slow process and cannot be considered real-time. In the 1970's, the emergence of fast electronic scanning by a 2D probe made real-time imaging possible but made extended field of views more difficult. Yet there

* 3D error = $\sqrt{(\text{error\_x})^2 + (\text{error\_y})^2 + (\text{error\_z})^2}$

continues to be a clinical interest in extended field-of-view so manufacturers have recently developed panoramic techniques using 2D probes. The panorama is created by sweeping the probe in the lateral direction over a region of interest. Examples of such systems are Siescape (Siemens Medical Systems, NJ, USA) and LOGIQView (GE Medical Systems, Waukesha, WI, USA) (Forsberg 2004). These modern techniques stitch a series of images together using fast digital signal processors (Tirumalai et al. 1997). Normally, spatial compounding, which averages the signal intensities in the overlapping areas, is applied to improve the signal-to-noise ratio (Appendix E). The key issue is the alignment of the images so that the anatomical features are not distorted. Most of the modern systems align the images using the features within the images and do not use an external position tracker.

As mentioned, 3D ultrasound can be created in an analogous manner by sweeping the probe in the elevation direction, similar to stacking a deck of cards. The dimensions of the volume are determined by the freehand motion of the operator so an extended 3D volume is possible. Many such 3D systems have been created using a variety of position trackers to measure the location of each image (Fenster and Downey, 1996). Key issues are image alignment and speed of reconstruction (Rohing et al. 1998; Edwards et al. 1998, Edwards 1999). Systems have also been developed without a position tracker by using again the image-content to provide an estimate of the alignment of the set of images. A commercial example is 3Scape (Siemens Medical Systems, NJ, USA). Whether or not a tracking sensor is used, the elevation resolution of the extended volume is typically worse than the axial and lateral resolutions. Therefore re-slices of the extended volume in the elevation direction often have poor image quality. Spatial compounding can improve image quality but requires repeated scanning of the region from different points of view (Rohling et al. 1997). This increases the acquisition time making the results more susceptible to patient motion.

The result is that freehand 3D ultrasound is rarely used for panoramic imaging. The dedicated 3D probes aim to produce high quality 3D images in all directions (axial, lateral and elevational) with fast acquisition rates. Examples are the Voluson 730 (General Electric Medical Systems, Waukesha, WI, USA) and iU22 (Philips Medical Systems, MA, USA). The two examples are capable of generating real-time ultrasound

volumes, but the probes have different acquisition mechanisms. The Voluson probe uses a motor inside the probe to rotate an array of piezoelectric transducer elements in a sweeping motion. This method creates a stack of images that are reconstructed into a single volume. This processes is repeated at a rate determined by the motor. The iU22 probe contains a 2D phased array with 2800 elements. This 2D array permits focusing in the elevation plane for volume acquisition (Forsberg, 2004). Other commercial 3D probes follow designs similar to these two examples. Compared to freehand systems, these dedicated 3D systems offered a faster acquisition rate but do not provide the capability for an extended field of view.

The next obvious evolutionary stage is to stitch the volumes together from a dedicated 3D machine into a panorama. This technique would combine the benefits of a high-quality 3D image with an extended view of the anatomy. This paper describes the development of a system to measure the calibrated position of the probe, acquire multiple volumes and register the volumes together. The key, as before, is the registration step that aligns the overlapping regions. The challenge is to accommodate the various sources of error including speed of sound variations, refraction, patient motion and miscalibration of the position tracker. Some of these errors can be described by rigid-body motion, others are non-rigid. Both rigid body and warping-based registration techniques will be considered. It is expected that the extended volumes will maintain the good image quality in the elevational direction, and that acquisition time will be short.

From a clinical perspective, a 3D extended field-of-view provides sonographers the flexibility to visualize anatomical structures from a variety of different angles instead of mentally interpreting the 3D structure from 2D images (Peetrons 2002; Leung et al. 2005). An extended field-of-view (both 2D and 3D) also provides a better demonstration of the spatial relationships among structures when the size of a single volume is not large enough to cover the structures (Kim et al., 2003). Given a global perspective of the examination area, the sonsographer can identify individual structures easier (Dietrich et al., 2002). This also implies that referring or non-examining doctors can interpret panoramic volumes easier because more features are visible compared to a single view (Henrich et al., 2003). The extended views are also similar to the full views available from MRI or CT. Another advantage is that accurate distance or size measurements of

large organs are possible (Ying and Sin, 2005; Kim et al., 2003). The use of ultrasound extended field-of-view in clinical practice appears in many applications. Table 1-1 lists samples of the publications that describe the benefits of extended field-of-view for examination and documentation.

Table 1 - 1 : Applications of extended field-of-view ultrasound

Body systems	Organs or cases	Applications
Abdominal	(Multiple organ study by Kim et al. (2003) and Dietrich et al. (2002))	• Illustrate the anatomical context of the lesion in its surroundings. • Provide precise measurement and tracing of the extended and tubular structures. • Improve the accuracy and reproducibility of measurements in the examination of larger structures and organs. • Increase understanding and acceptance by referring clinicians.
Lymphatic	Lymph nodes of the neck (Beissert et al. 2000)	• Detect cervical lymphadenopathy reliably.
Musculoskeletal	Neck muscles around cervical spine (Leung et al. 2005)	• Visualize the musculoligamentous structures, especially the posterior neck muscles.
	Multiple abnormal cases in different areas (Lin et al. 1999)	• Measure and display abnormalities (most often fluid collections or masses and extra-articular extremity abnormalities).
	Shoulder arthroplasty (Sofka and Adler 2003)	• Improve visualization of regional anatomic landmarks.
Neurological	Neurosurgical intra-operative sonography (Woydt et al. 2001)	• Image the entire tumor using small phased-array probes. • Measure the diameter of the tumor reliably. • Perform a comprehensive comparison

		with trancranial ultrasound or MR.
Reproductive	Obstetrics and gynecology (Henrich et al. 2002a, 2003; Baba et al. 1999)	• Visualize the uterus in its entirety as well as genital tract tumors, the placental implantation and fetal structures throughout pregnancy. • Provide documentation of surroundings and topographic orientation in large pelvic masses and findings that exceed the limitations of conventional real-time scans.
	Placenta percreta (Henrich et al. 2002b)	• Diagnose a placenta percreta in a woman infected with the human immunodeficiency virus (HIV).
Urinary	Urinary tract (Riccabona 2002)	• Improve measuring large organs (e.g., large transplant kidneys, megacystis, large tumours or malformations). • Improve visualizing complex and large pathology (e.g., from the kidney to the urinary bladder).
Multiple body systems (Sauerbrei 1999)	(various)	• Measure large structures. • Reveal the anatomic context of abnormalities when conventional real-time scans are not applicable.

1.3 Ultrasound Artifacts

Artifacts in medical imaging represent any incorrect features that are shown on the image of the anatomical body. They are usually caused by the undesired aspects of the imaging technique and affect the diagnostic information. This section provides a brief overview of some common ultrasound artifacts (Rohling 1998, Kremkau 2002). Some artifacts affect probe calibration and extended field-of-view and will be mentioned in the following chapters. It is also important to realize that artifacts bring challenges to the

interpretation of ultrasound images. For this reason, ultrasound imaging requires operators who are highly-skilled in both image acquisition and interpretation (Wells, 2000).

1.3.1 Beam Thickness

Figure 1-1 illustrates that an ultrasound volume is composed of a stack of 2D images. These image planes appear thin but the echoes to create the images actually originated from an ultrasound beam with finite thickness (Figure 1-2). The ultrasound beam is typically thickest in the elevational direction. Objects that are slightly off the center of the beam can reflect echoes back to the probe. This type of off-center reflection causes blurring in the elevational direction and therefore, the resolution in this direction is lower than the axial and the lateral resolutions.

For the 3D probe used in this thesis, the elevation resolution is also non-uniform. Given the fan-shaped acquisition, resolution is worst at deep axial locations.

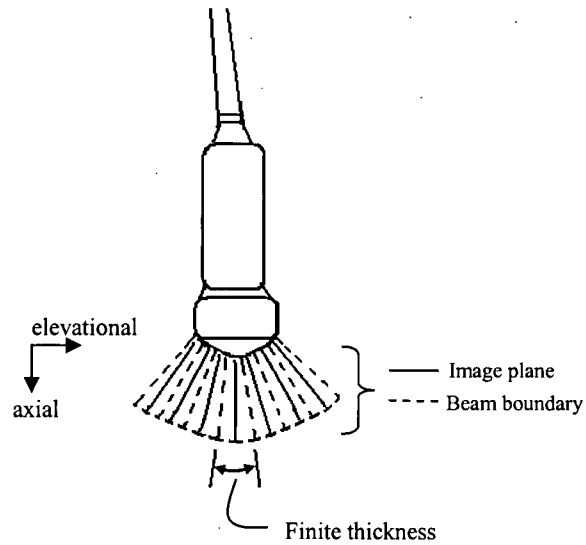

Figure 1 - 2 : Each image plane is produced by the echo of the ultrasound beam with finite thickness. (The number of image planes on the figure is fewer than that on the actual probe.)

1.3.2 Speckle

The grainy appearance of ultrasound images is due to the existence of speckle (Figure 1-3). The echo pattern received from the probe does not only come from direct reflection from the tissue texture, but in fact, represents the accumulation of interference effects from many tiny scatters that constitute the tissue. The probe is constructed by an array of piezoelectric elements responsible for exciting ultrasound pulses and for receiving echoes. These elements fire their pulses together and wait for the echoes back. For this reason, speckle exists in all ultrasound images, although it can be reduced by digital filtering techniques (Guo 1999, Dantas et al. 2002, Loizou et al. 2002, Evans and Nixon 1993).

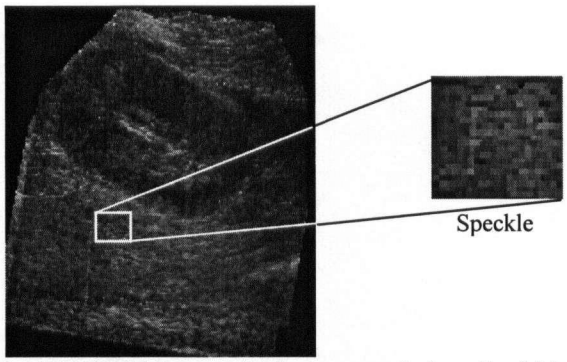

Figure 1 - 3 : An image of a human kidney – the large area below the kidney clearly depicts speckle (grainy appearance).

1.3.3 Reverberation

Reverberation occurs in the presence of a strong reflector with the tissue. The strength of the reflector can create multiple echoes traveling back and forth between the reflector and the surface of the probe, a multiple reflecting surface in the tissue (Figure 1-4). The multiple echoes appear as repeated bright regions in the image. The material of the probe face is also a factor of this artifact. The acoustic impedance of the probe face should match with that of human skin to avoid echo reflections the probe and skin. The use of coupling gel usually helps to reduce this effect.

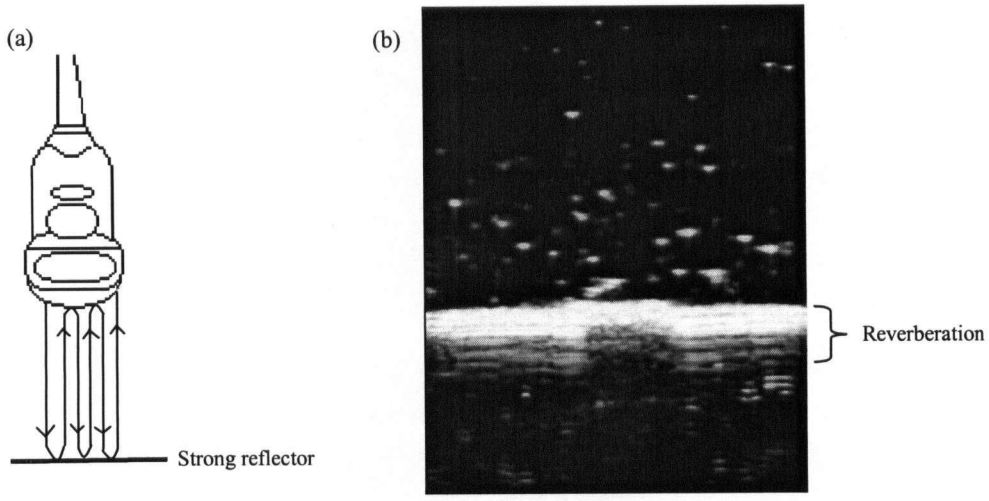

Figure 1 - 4 : (a) A pulse is transmitted from the probe to the strong reflector and a strong echo is reflected back to the probe. However, the echo is only partially absorbed by the probe and is reflected to the reflector again. The back and forth traveling of the pulse causes reverberation. (b) The effect of reverberation when a probe images the flat bottom of a water bath. Multiple layers of the bottom appear on the image, but only the top layer represents the true distance between the probe surface and the bottom.

1.3.4 Refraction

Acoustic refraction results in incorrect positioning of a reflector on the image due to a wavelength change in the ultrasound path. Similar to light refraction, the direction of the ultrasound beam changes at the boundary between two regions with different acoustic impedances (Figure 1-5). The effect of refraction causes misplacements of the anatomical structures.

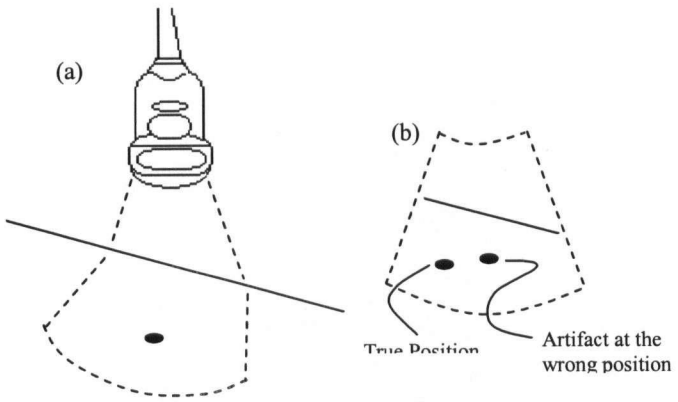

Figure 1 - 5 : (a) The direction of the ultrasound beam is shifted by refraction. (b) The position of the reflector (black dot) is located at the wrong location in the image.

1.3.5 Speed Error

To compute the position of an anatomical structure on the image, the elapsed time of the echoes and the propagation speed of the ultrasound pulses are combined. Most ultrasound scanner uses 1540 m/s as the propagation speed but this speed is not a constant throughout the human body. The speed of sound in soft tissue can vary by as much as 14% (Hill et al. 2004). This can cause an error in displacing structure in the axial direction of the ultrasound beam. If the actual propagation speed is greater than the assumed speed (1540 m/s), the calculated distance of the reflector will appear to be too close to the probe. If the actual propagation speed is less than the assumed speed, the reflector will be placed too far from the probe. Both refraction and the propagation speed errors can cause a structure to appear deformed from its true shape.

1.3.6 Attenuation

The strength of an ultrasound pulse attenuates along its path of travel in the human tissue. The amplitude of any anatomical feature on the image depends on the signal strength of the echoes received by the probe. However, in the presence of attenuation, deeper echoes are normally amplified more than shallow echoes using a logarithmic scale, so that theoretically the echo amplitude is normalized with depth. There are two types of artifacts regarding attenuation – shadowing and enhancement (Figure 1-6). Shadowing and enhancement refer to structure depicted in the image with a brightness that is too low and too high, respectively. Shadowing is the weakening of the echo amplitude because there is a strongly reflecting or attenuating structure blocking a significant portion of the ultrasound energy from propagating further. Any structure lying behind this structure can only be detected by weak ultrasound echoes. For this reason, it appears darker, like a shadow on the image. Enhancement is the opposition of shadowing. A portion of ultrasound beam travels to a deep region with very little attenuation. Any deep-lying structure is exposed to stronger ultrasound pulses than expected and it appears brighter in the image. Although considered artifacts, enhancement and shadowing can actually aid the analysis of suspicious masses in the body.

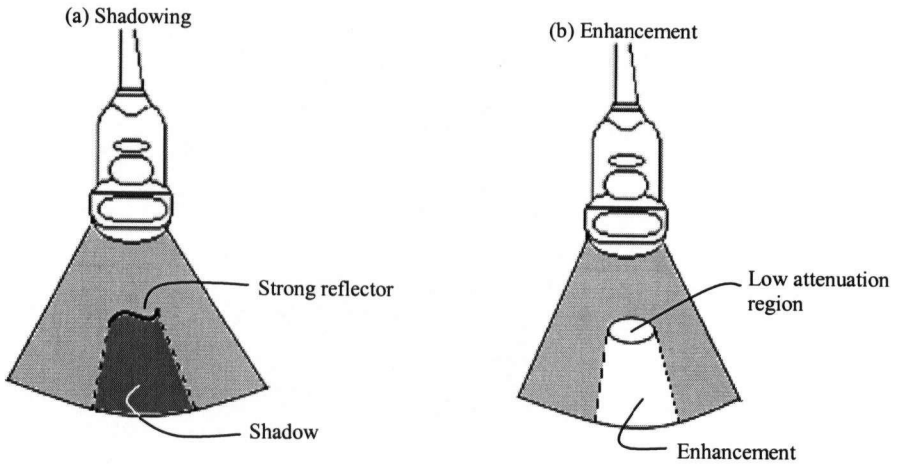

Figure 1 - 6 : (a) Shadowing – most of the ultrasound beam reflects at the strong reflector and the region behind the reflector is barely detected by the weaker beam. (b) Enhancement – the region behind an area with low attenuation is enhanced by a stronger beam.

1.4 Thesis Overview

This thesis presents a comparison of 3D probe calibration methods, chooses the best method, and then applies it to the extended field-of-view application. The extended field-of-view method describes a new registration method to improve the depictions. The thesis is organized into four chapters.

Chapter 2 describes the calibration mathematics and gives a literature review of related work. The study of 3D probe calibration investigates three methods. Each method requires a specific mathematical model and the algorithms to solve them are presented within a common mathematical framework. The calibration results are verified by a number of tests, including calibration reproducibility, point accuracy and reconstruction accuracy by distance measurement. These tests are useful for determining the performance of each method.

Chapter 3 derives the methods for volume extended field-of-view. We are the first to develop extended field-of-view with dedicated 3D probes using the previous probe calibration results. Multiple volumes are registered into a common space to produce an extended volume. A new registration technique is developed for improving the matching among overlapping regions. Two other less complicated techniques are

presented to provide alternatives for the reconstruction of extended volumes. Tests are performed *in vitro* and *in vivo* to analyze the methods. Results from each method are compared in a number of areas – reproducibility, similarity measure in the overlapping regions, and distance measurement.

Chapter 4 summarizes the progress and presents future work. It describes why the work in this thesis deserves attention for potential clinical applications and introduces some topics for future work.

Chapter 2 Probe Calibration

Probe calibration determines the transformation between the coordinate systems of the sensor and the ultrasound volume. The sensor is normally attached to the probe handle. In this way, the position and the orientation measurements of the probe by the tracking system can be converted into the position and orientation of the ultrasound volumes. The chosen tracking system is an optical 3D measurement system (Optotrak 3020, Northern Digital Inc., Waterloo, Canada) with three cameras. The three-camera system detects the IRLED (infrared light emitting diode) sensors placed on the probe to calculate the position and orientation of the probe using the theory of stereo imaging (Forsyth and Ponce, 2003). The manufacturer reports that the RMS accuracy of a measurement at 2.25 m distance is equal to 0.1 mm for the x, y coordinates (parallel to the focal planes of the cameras) and 0.15 mm for z coordinate (distance from the camera). These numbers were confirmed by an external study that also reports 0.15 mm RMS accuracy (Rohling et al. 1995). The maximum frame rate to determine a 3D measurement is 450 Hz.

2.1 Calibration Procedure

The probe calibration is expressed as a rigid-body transformation, ${}^{P}\mathbf{T}_{V}$, between the coordinate systems of the ultrasound volume (V) and the probe (P). Calibration is performed with the use of a phantom, an artificial object. Three coordinate systems are established as listed below and shown in Fig. 2-1:

- **Box** (***B*** or ***G***). The phantom box (B) coordinate system is defined on its outer wall facing the position tracking system. This coordinate system is intended to replace the conventional reference frame defined by the tracking system. After the tracking system measures the positions of sensors attached on the wall, it determines the position and orientation of this coordinate system. The phantom box is firmly attached on an experiment table with two iron C-clamps so its coordinate system remains spatially unchanged during the calibration procedure. It also serves as the

global coordinate system (G) of the tracking system ($B = G$) . It is more convenient to use the box as the global coordinate system instead of the base of the tracking system, because all coordinate system transformations will have the same order of magnitude.

- **Probe (*P*).** The probe's coordinate system is defined by the sensors on the probe handle. The tracking system measures the positions of the sensors in realtime to determine the position and orientation of the probe.
- **Volume (*V*).** The ultrasound volume coordinate system follows the row-column-slice (i, j, k) index scheme to specify the positions of voxels in the 3D data set. The origin and axes are located at a top corner of the volume, near the probe head. The axes of the system represent the three directions of the ultrasound echo signals. The x-axis is in the lateral direction, the y-axis is in the axial (beam) direction and, finally, the z-axis is in the elevation direction.

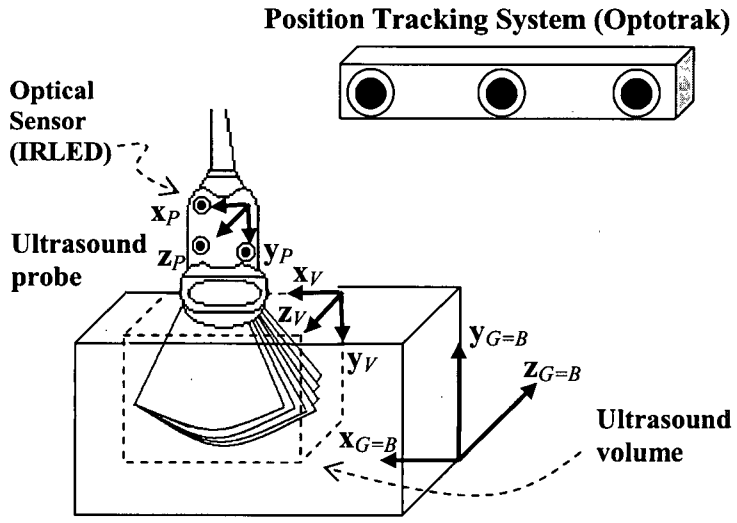

Figure 2 - 1 : The coordinate systems used to determine ${}^{P}T_{V}$. Note that the optical tracking system is always placed on a fixed stand above the examination table, to give a clear line of sight from the sensors (IRLED) to the three cameras on the tracking system. The global [$x_{G=B}$, $y_{G=B}$, $z_{G=B}$], ultrasound probe [x_P, y_P, z_P] and ultrasound volume [x_V, y_V, z_V] coordinate systems are also shown. The global coordinate system is determined by IRLED markers on the wall of the phantom.

The transformation between a pair of coordinate systems can be expressed mathematically as a homogeneous transformation matrix. Appendix A illustrates the

principles of rigid-body transformation and presents the derivation of the homogeneous transformation matrix. The matrix is formed by six parameters, three for translation and three for rotation. The translation part (x, y, z) specifies the position of one coordinate system relative to another, whereas the rotation part (α, β, γ) specifies the orientation. A Roll-Pitch-Yaw angle scheme for the α-β-γ angles is adopted. The relative orientation of the coordinate system is described by first rotating through γ around the x-axis, then through β around the y-axis and, finally, through α around the z-axis. The transformation matrix is represented as follows:

$$ {}^{P}\mathbf{T}_{V} = \begin{bmatrix} \cos\alpha\cos\beta & \cos\alpha\sin\beta\sin\gamma - \sin\alpha\cos\gamma & \cos\alpha\sin\beta\cos\gamma + \sin\alpha\sin\gamma & x \\ \sin\alpha\cos\beta & \sin\alpha\sin\beta\sin\gamma - \cos\alpha\cos\gamma & \sin\alpha\sin\beta\cos\gamma - \cos\alpha\sin\gamma & y \\ -\sin\beta & \cos\beta\sin\gamma & \cos\beta\cos\gamma & z \\ 0 & 0 & 0 & 1 \end{bmatrix} \tag{2-1} $$

To transform a voxel (i,j,k) in V to P, the following equation is used:

$$ \begin{bmatrix} {}^{P}x \\ {}^{P}y \\ {}^{P}z \\ 1 \end{bmatrix} = {}^{P}\mathbf{T}_{V} \begin{bmatrix} {}^{V}x \\ {}^{V}y \\ {}^{V}z \\ 1 \end{bmatrix} = {}^{P}\mathbf{T}_{V} \begin{bmatrix} s_X \cdot i \\ s_Y \cdot j \\ s_Z \cdot k \\ 1 \end{bmatrix} \tag{2-2} $$

where (s_X, s_Y, s_Z) are the spatial dimensions of the voxel in physical space with units of mm/voxel, (${}^{V}x$, ${}^{V}y$, ${}^{V}z$) is the voxel location in units of mm and (${}^{P}x$, ${}^{P}y$, ${}^{P}z$) is the transformed position of a voxel with respect to the probe's coordinate system. The values of (s_X, s_Y, s_Z) are supplied by the ultrasound machine and depend on the acquisition configuration, including the selected image depth. With ${}^{P}\mathbf{T}_{V}$ found by calibration and the system P measured with respect to G by the tracker (${}^{G}\mathbf{T}_{P}$), the position of an anatomical target inside an ultrasound volume can be computed in global coordinates using

$$ {}^{G}\mathbf{x} = {}^{G}\mathbf{T}_{p}\,{}^{P}\mathbf{T}_{V}\,{}^{V}\mathbf{x} \tag{2-3}. $$

The objective of this study is to analyze three probe calibration methods for calculating ${}^{P}\mathbf{T}_{V}$ for a 3D probe. There has been considerable previous research into probe calibration but almost all previous work describes methods for standard 2D probes. For 2D probes, the transformation equations are similar, except that the coordinate system V describes the top corner of the 2D ultrasound image instead of the volume.

For 2D probe calibration, the procedure to determine the six parameters of the transformation matrix usually requires five steps:

1. Construct a phantom with known or measured geometrical properties.
2. Acquire one or more 2D ultrasound images of the phantom and measure the position and orientation of attached sensors on the probe in the global coordinate system.
3. Identify the features of the phantom in the ultrasound image that correspond to the phantom geometry.
4. Construct transformation equations that match the known and identified features in terms of the six calibration parameters.
5. Solve the six unknown parameters from a set of transformation equations using least-square or nonlinear fitting methods.

3D calibration will follow a similar set of steps.

2.2 Acquisition System

The acquisition system consists of a 3D ultrasound scanner (Voluson 730 Pro, GE Medical Systems, Waukesha, WI, USA) and the Optotrak system. A dual Pentium III 1.0 GHz processor computer is used to record the sensor measurements. Ultrasound volumes are acquired with a 4-8 MHz curved array 3D probe. The piezoelectric elements of the probe are arranged in a convex array to capture 2D images. The array is attached to a motor inside the probe head, so that 3D volumes are constructed by moving the array in a sweeping motion (see the fan shape in Fig. 2-1). All ultrasound volumes acquired from the Voluson 730 Pro in this study have the following geometrical properties: 6.8 cm axial

depth, 45° sweep angle, 199(lateral) x123(axial) x105(elevation) voxels in size and 0.43 mm/voxel scaling factor ($s_X = s_Y = s_Z$). They are transferred from the ultrasound machine to the computer workstation through a proprietary software package from GE Medical Systems called 3DView2000. 3DView2000 uses the DICOM (Digital Imaging and Communications in Medicine) standard. The automatic algorithms to solve the transformation matrix in each calibration method were developed in C++ (Visual Studio, Microsoft Corporation, Redmond, WA, USA) and Matlab (Mathworks, Inc, Natick, MA, USA). In addition, a commercial visualization tool, Amira (Mercury Computer Systems, Chelmsford, MA, USA), was used to perform ultrasound volume registration for the IXI-wire method

The optical tracking system is used to track both the 3D probe and a tracking stylus. For both devices, a number of infrared light emitting diodes (IRLEDs) are placed on each instrument to measure its position and orientation in 3D space with respect to the cameras. A preliminary set-up procedure for each device is required to define a coordinate system (origin and axes) based on the IRLEDs. There are four IRLEDs fixed rigidly on the stylus and eight IRLEDs on the ultrasound probe.

The stylus has two purposes in the study, one for measurement of phantom geometry, and the other for probe calibration itself. In particular, the stylus is used to measure the geometrical properties of the phantoms in the IXI-wire and cube methods and is used in lieu of a phantom for the stylus method. There are two types of tips to serve the two purposes. A stylus with a sharp tip is used as a measuring pointer to accurately determine the tip position. A stylus with a bead tip is used for calibration, where the tip needs to be clearly visible in the ultrasound volume.

In both cases, the position of its tip must be known with respect to the coordinate system of the IRLEDs. Thus, an extra preliminary calculation is performed to determine the vector from the origin of the stylus IRLED's coordinate system to its tip. The calculation of the vector to the tip uses a procedure where the stylus is pivoted about a stationary point at the tip. This procedure collects a variety of position measurements of the IRLEDs for various poses around the pivot. Since the tip cannot leave the pivot, the stylus is moved in a spherical fashion around the pivot. A least-squares fit of a sphere to the data determines the unknown vector position to the tip. This calibration was done

once for each type of stylus and the result was used for all tests. The residual RMS errors of this procedure are 0.12 mm and 0.23 mm for the sharp and bead tips, respectively.

2.3 Calibration Algorithms

Custom phantoms and semiautomatic feature detection algorithms were developed for solving the calibration problem for each of the three proposed methods. The algorithms match the feature points extracted from ultrasound volumes to their associated geometrical properties. From the matching features, the six parameters of the transformation matrix are calculated using the known geometry. The geometrical properties include **lines** for the IXI-wire method, **planes** for the cube method and **points** for the stylus method. Based on the calibration solutions computed by the three methods, these methods are verified in terms of their reproducibility of calibration results, accuracy of a known position and reconstruction accuracy of distances between two fixed points from two volumes. Prager et al. (1998) constructed phantoms based on points, lines and planes for 2D probe calibration and measured precision, accuracy and calibration reproducibility. That study suggested that planes were beneficial because of a redundancy of image features (many points make up a plane). The question is whether the same conclusion can be made for calibration of 3D phantoms.

2.3.1 Calibration Phantoms

For all calibration methods, a phantom is immersed in a warm water bath inside a rigid thermoplastic container during the ultrasound volume acquisition. This container is denoted as the phantom box. The water is maintained at a temperature of 37 ±1 °C (within the 10-40 °C operational range of Voluson), to approach the speed of sound used by the ultrasound machine (and to match s_X, s_Y, and s_Z). The temperature is monitored by a thermometer and is maintained by replenishing the water periodically. Figure 2-2 shows the phantoms.

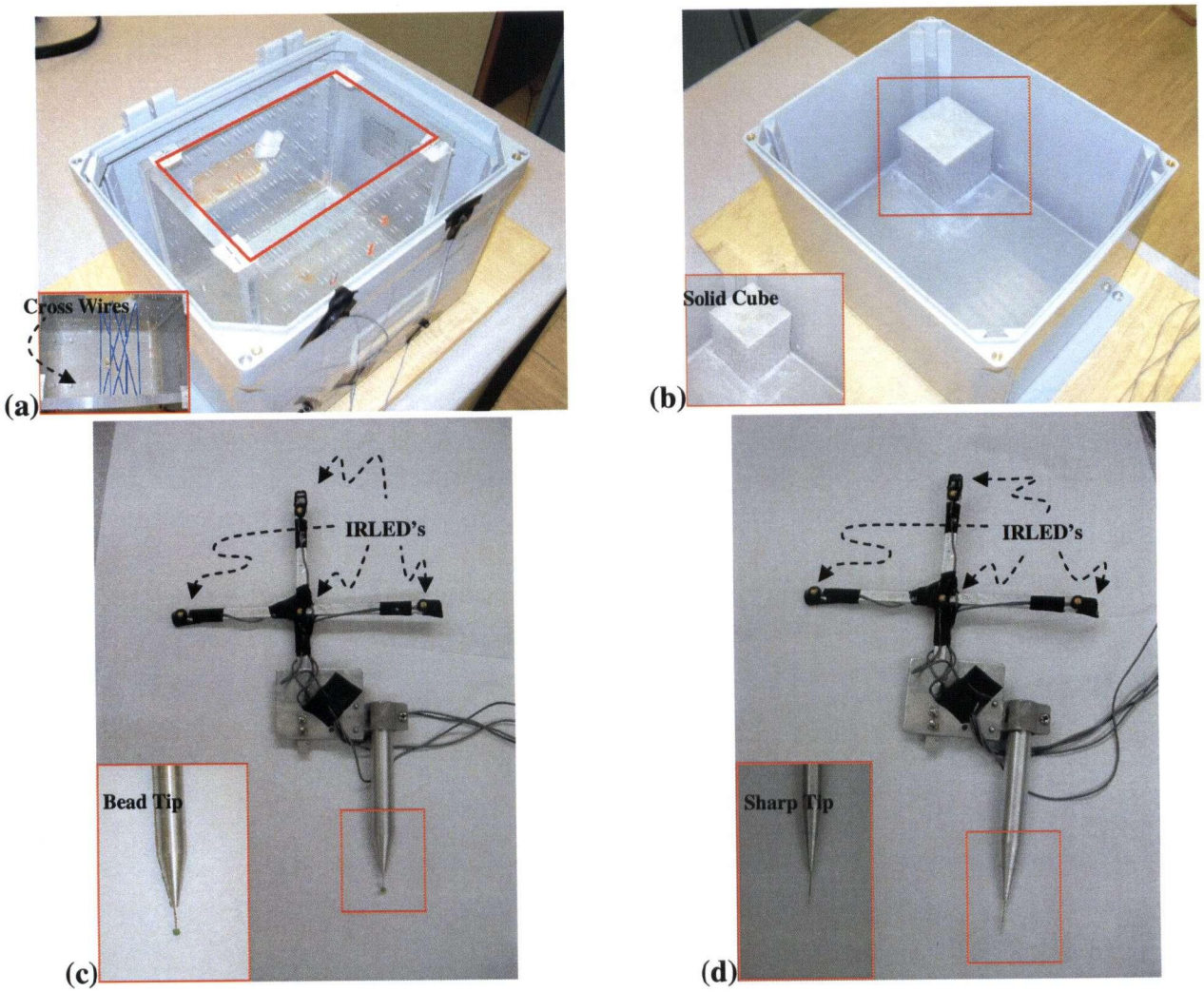

Figure 2 - 2 : (a) The IXI-wire phantom (the IXI-wires are highlighted with thick lines for the purpose of illustration.); (b) The cube phantom; (c) The stylus as a phantom with a bead tip; (d) The stylus as a measuring tool with a sharp tip to localize the position of any point in space.

The IXI-wire phantom is constructed with 0.28 mm nylon wires, crossing between two walls of the box. The shape of each layer resembles the three-letter combination "IXI." It is analogous to the N-wire phantom (Pagoulatos et al. 2001 and Comeau et al. 2000) except an additional wire is added to the letter "N" to create "IXI". The "N" shape guarantees that the mirror image registration is not possible, but a reasonable initial guess to the calibration eliminates this problem. The additional wire therefore adds additional features to aid the registration. There are two layers separated by 23 mm in depth. Figure 2-3 shows the IXI-wire configuration. The spatial positions of all wire end points are measured by the stylus.

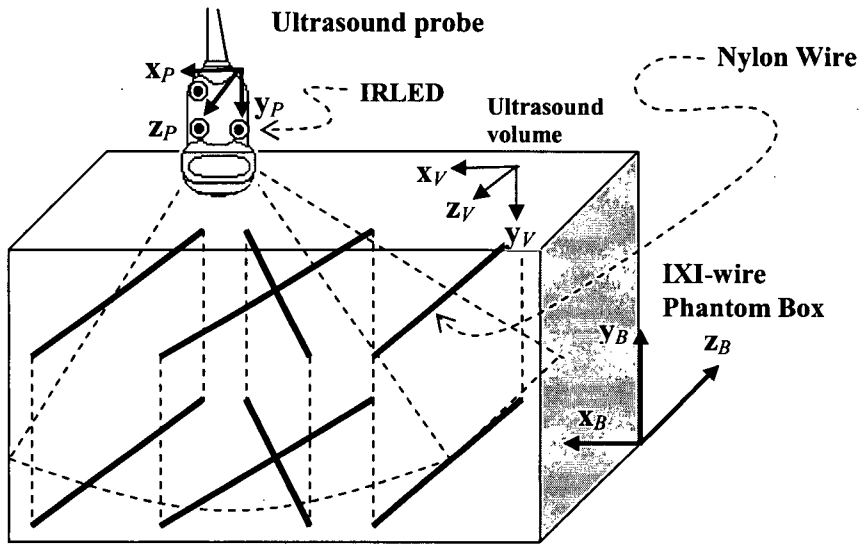

Figure 2 - 3 : The configuration of the three coordinate systems for calibration using the IXI-wire method. The ultrasound volume captures the two layers of IXI-wires. The phantom box [x_B, y_B, z_B], ultrasound probe [x_P, y_P, z_P] and ultrasound volume [x_V, y_V, z_V] coordinate systems are shown.

The cube phantom uses a solid cube (60 mm x 60 mm x 60 mm), accurately machined from aluminum. It is secured to an inner corner of the phantom box, such that three planes of the cube are visible by ultrasound. Scanning this phantom with the probe under water produces three clear, flat orthogonal planes in the ultrasound volume. Figure 2-4 shows the configuration.

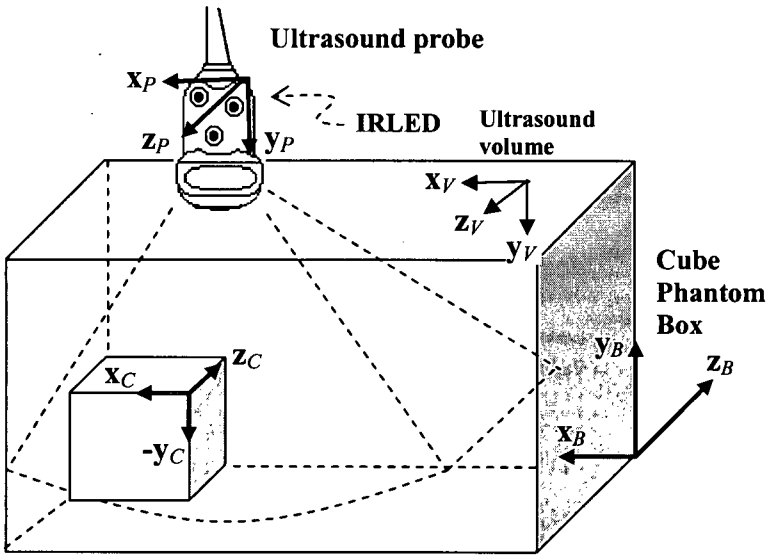

Figure 2 - 4 : The configuration of the four coordinate systems for calibration using the cube method. The ultrasound volume captures the three orthogonal planes of the cube. The phantom box [x_B, y_B, z_B], ultrasound probe [x_P, y_P, z_P], ultrasound volume [x_V, y_V, z_V] and cube [x_C, y_C, z_C] coordinate systems are shown.

The stylus calibration method uses the stylus with the bead at the tip. The vector from the coordinate system of the IRLEDs to the tip is known with respect to the center of the bead. The center of the spherical dot in the ultrasound volume therefore matches the center of the bead in the calibration equations. Figure 2-5 shows the configuration of the stylus system. A bright, sharp reflection of the bead sphere is produced in the ultrasound volume.

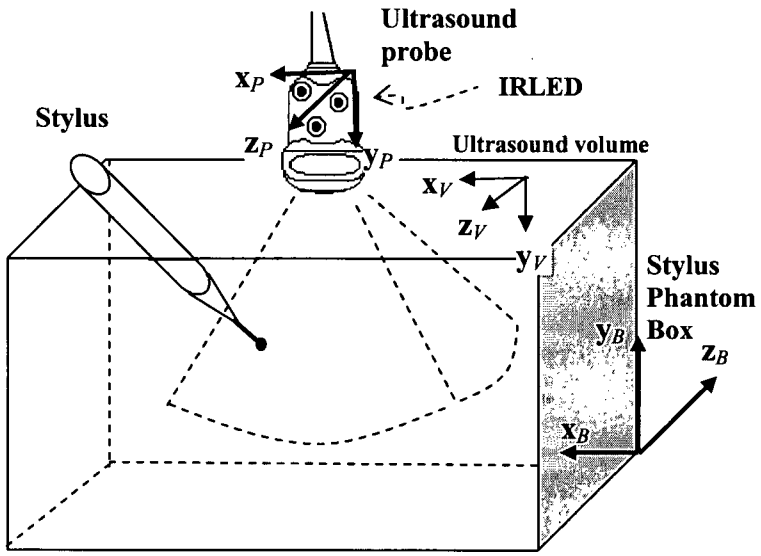

Figure 2 - 5 : The configuration of the three coordinate systems for calibration using the stylus method. The ultrasound volume captures the bead at the tip of the stylus. The phantom box [x_B, y_B, z_B], ultrasound probe [x_P, y_P, z_P] and ultrasound volume [x_V, y_V, z_V] coordinate systems are shown.

2.3.2 IXI-Wire Calibration Equations

IXI-wire calibration requires three coordinate systems to describe the calculation of the calibration matrix. The relationship between coordinate systems can be represented by three transformation matrices (Appendix A), ${}^{B}\mathbf{T}_{V}$, ${}^{B}\mathbf{T}_{P}$ and ${}^{P}\mathbf{T}_{V}$. ${}^{P}\mathbf{T}_{V}$ is the transformation from ultrasound volume to the ultrasound probe coordinate system, ${}^{B}\mathbf{T}_{P}$ is the transformation from the probe to the phantom box coordinate system and ${}^{B}\mathbf{T}_{V}$ is the transformation from the ultrasound volume to the phantom box coordinate system. This method requires only a single ultrasound volume for calibration. The matrix equation of the calibration problem is

$$ {}^{B}\mathbf{T}_{V} = {}^{B}\mathbf{T}_{P}\,{}^{P}\mathbf{T}_{V}. \tag{2-4} $$

${}^{B}\mathbf{T}_{P}$ is measured by the Optotrak with a minimum of three IRLEDs on the probe and three on the box. ${}^{B}\mathbf{T}_{V}$ is determined in two steps. First, construct a reference 3D data structure of the IXI-wire model to describe the physical geometry of the wires. This reference

structure is based on the coordinate system of the box. Second, register the ultrasound volume of the IXI-wire phantom with the reference data structure. The solution of the registration produces the six translation and rotation parameters of ${}^{B}\mathbf{T}_{V}$. ${}^{P}\mathbf{T}_{V}$ is determined by the following equation, when ${}^{B}\mathbf{T}_{V}$ and ${}^{B}\mathbf{T}_{P}$ are known:

$$ {}^{P}\mathbf{T}_{V} = ({}^{B}\mathbf{T}_{P})^{-1}\,{}^{B}\mathbf{T}_{V}. \tag{2-5} $$

The registration between the data structure and the ultrasound volume is based on maximization of a similarity measure. In particular, the algorithm uses the intensity information of each voxel in the overlapping regions of the two datasets to calculate the correlation coefficient (Appendix B). The algorithm iterates over the six translation and rotation parameters until the correlation coefficient reaches a maximum. The final values of the parameters are taken as the optimal alignment ${}^{B}\mathbf{T}_{V}$. The Amira toolkit is used to perform the registration and this uses a gradient descent technique. Figure 2-6 shows an example of the registration process.

When ${}^{B}\mathbf{T}_{V}$ is computed by volume registration and ${}^{B}\mathbf{T}_{P}$ is measured by the Optotrak, ${}^{P}\mathbf{T}_{V}$ is computed by eqn (2-5). ${}^{P}\mathbf{T}_{V}$ therefore takes the form of

$$ {}^{P}\mathbf{T}_{V} = \begin{bmatrix} r_{11} & r_{12} & r_{13} & r_{14} \\ r_{21} & r_{22} & r_{23} & r_{24} \\ r_{31} & r_{32} & r_{33} & r_{34} \\ 0 & 0 & 0 & 1 \end{bmatrix}. \tag{2-6} $$

Given a homogeneous transformation matrix, as in eqn (2-6), the translation (x, y, z) and the rotation parameters (α, β, γ) are extracted as follows (Sciavicco and Siciliano, 2004):

$$ \alpha = \tan^{-1}\left(\frac{r_{21}}{r_{11}}\right) \qquad \beta = \tan^{-1}\left(\frac{-r_{31}}{\sqrt{r_{32}^2 + r_{33}^2}}\right) \qquad \gamma = \tan^{-1}\left(\frac{r_{32}}{r_{33}}\right) $$

$$ x = r_{14} \qquad y = r_{24} \qquad z = r_{34} \tag{2-7} $$

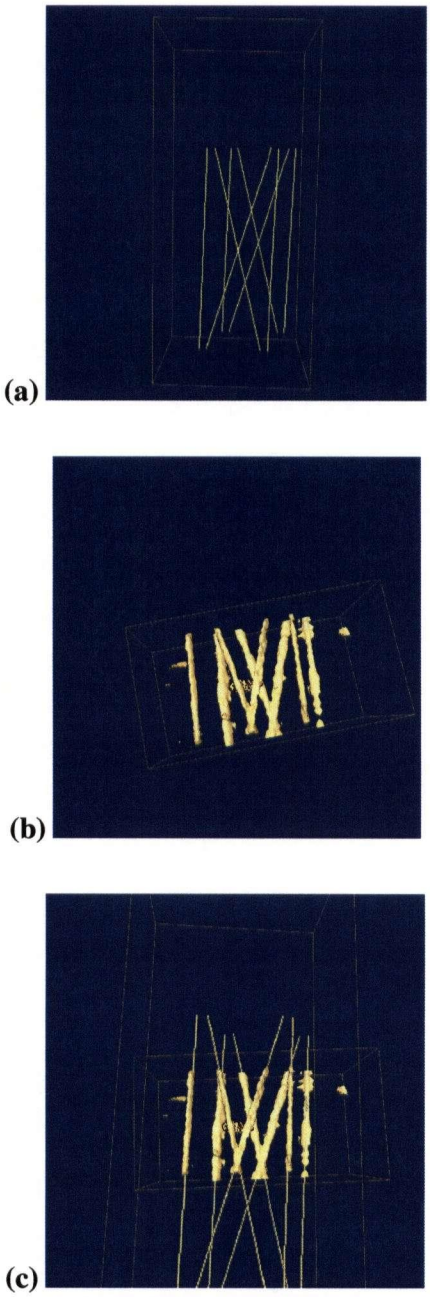

Figure 2 - 6 : The registration of the ultrasound volume to the reference data set. (a) The reference data structure that describes the configuration of the wires. (b) A volume rendering of an ultrasound volume of the IXI-wire phantom. (c) The registration between the two data sets aligns the features and determines the transformation between the volume (*V*) and phantom box (*B*). Note that the volume rendering is for illustration purposes only and does not depict all of the features and noise. The raw ultrasound data are used in registration (Images are generated by Amira (TGS Inc., San Diego, CA, USA))

2.3.3 Cube Calibration Equations

Cube calibration requires four coordinate systems to calculate the calibration matrix. These are the phantom box (B), the ultrasound probe (P), the ultrasound volume (V) and the cube phantom (C). The descriptions of the first three are identical to those of the ones in the IXI-wire method. The cube coordinate system (C) places the origin at the cube corner, and its axes lie along the three orthogonal edges from the origin, as shown in Fig.2-4. All optical tracking measurements are made relative to the phantom box coordinate system (B). Similar to the IXI-wire method, the cube method also uses a single ultrasound volume to determine the calibration matrix. The three planes of the cube appear as detectable flat surfaces in the ultrasound volume. A segmentation algorithm is developed to identify the three orthogonal planes in the volume and then the positions of the planes are used to solve the calibration. The segmentation begins by considering the volume data set as a stack of parallel slices and then 2D edge detection is performed on each slice to identify the ultrasound reflection with the cube faces. In particular, the Canny edge detection algorithm is used in Matlab (Canny 1986). Figure 2-7 shows an example of the plane identification and Figure 2-8 describes the semiautomatic segmentation. Some gaps are apparent because those images planes with reverberation artifacts are not used for edge detection. Small gaps do not affect the result of calibration, as long as there are sufficient numbers of voxels to identify each plane.

The calibration equations are based on ${}^{C}\mathbf{T}_{B}$, ${}^{B}\mathbf{T}_{P}$ and ${}^{P}\mathbf{T}_{V}$. For the *x*-*z* plane on the top of the cube in the cube coordinate system (C), a voxel $({}^{V}x, {}^{V}y, {}^{V}z)$ that lies on this plane should satisfy:

$$\begin{bmatrix} {}^{C}x \\ 0 \\ {}^{C}z \\ 1 \end{bmatrix} = {}^{C}\mathbf{T}_{B}\,{}^{B}\mathbf{T}_{P}\,{}^{P}\mathbf{T}_{V} \begin{bmatrix} {}^{V}x \\ {}^{V}y \\ {}^{V}z \\ 1 \end{bmatrix}. \tag{2-8}$$

The left-hand side of eqn(2-8) becomes $[{}^{C}x\ {}^{C}y\ 0\ 1]^{T}$ for the *x*-*y* plane and $[0\ {}^{C}y\ {}^{C}z\ 1]^{T}$ for the *z*-*y* plane.

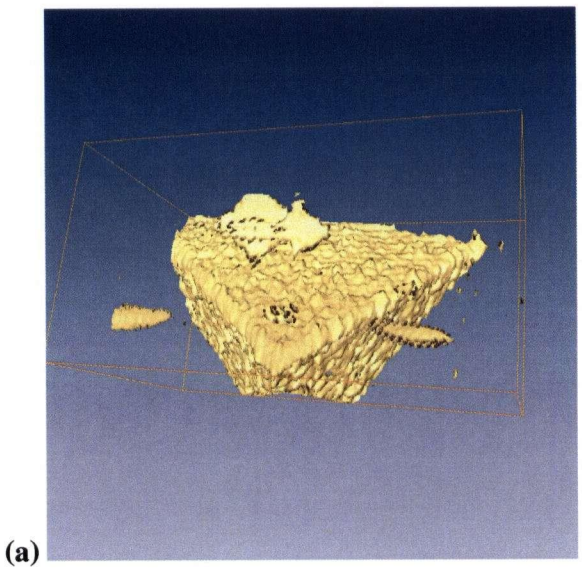

(a)

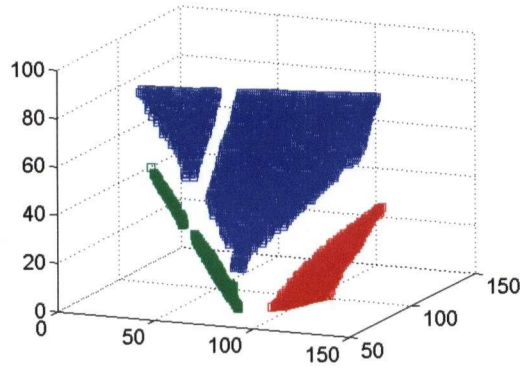

(b)

Figure 2 - 7 : The identification of voxels lying on the surface of the cube phantom. (a) A volume rendering of an ultrasound volume of the cube. The horizontal line segments on the left and the right sides are reverberation artifacts that are not used for plane segmentation. (b) The positions of the voxels lying on the surfaces planes are identified by edge detection.

As stated in the IXI-wire method, ${}^{B}\mathbf{T}_{P}$ is measured by the Optotrak. ${}^{C}\mathbf{T}_{B}$ is found by using the stylus to measure the spatial properties of the cube planes in the phantom box coordinate system. The zero component of each equation gives one equation to solve the six unknown parameters in the calibration transformation matrix, ${}^{P}\mathbf{T}_{V}$. There are hundreds of voxels that depict the three planes. By using these voxels, a set of over-determined equations are established from which to solve ${}^{P}\mathbf{T}_{V}$. The six parameters of ${}^{P}\mathbf{T}_{V}$ are determined from the set of equations by the Powell dogleg nonlinear iterative

optimization algorithm (Powell, 1970) with ${}^{C}\mathbf{T}_{B}$, ${}^{B}\mathbf{T}_{P}$ and $[{}^{V}x, {}^{V}y, {}^{V}z\ 1]^{T}$ as known inputs. For solving a set of N nonlinear equations with a vector of N unknowns, Powell's method starts at an initial point in N-dimensional space, and proceeds iteratively in each of the vector directions to reach the minimum error. Powell's method is preferred over Gauss-Newton or Levenberg-Marquardt methods when the initial guess may be far from the solutions and the Jacobian may have singularities.

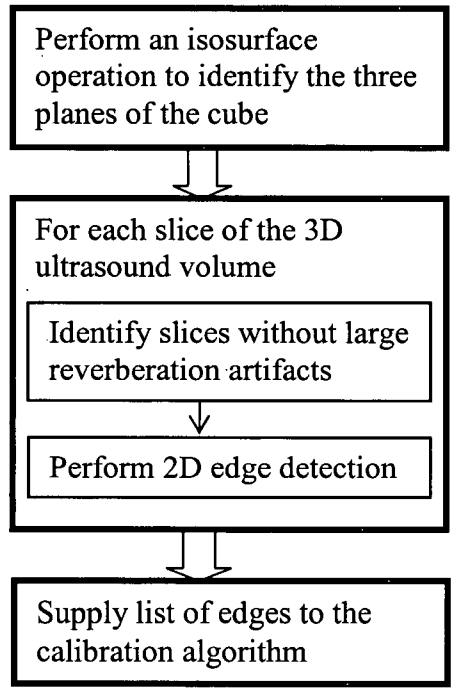

Figure 2 - 8 : The segmentation procedure to identify the positions of the cube planes in the ultrasound volume.

2.3.4 Stylus Calibration Equations

The stylus calibration uses the position of the bead at the tip to perform calibration. A number of ultrasound volumes are acquired of the stylus at different positions. For each ultrasound volume, the stylus tip is identified by a segmentation algorithm developed in Matlab. The segmentation algorithm identifies the tip of the stylus by processing the isosurface of the volume. By selecting a suitable threshold value above the background

noise level, the spherical bead at the tip is segmented. Figure 2-9 shows an example of the isosurface and Figure 2-10 describes the procedure of the segmentation. The center of the bead is then calculated from the centroid of the isosurface of the bead.

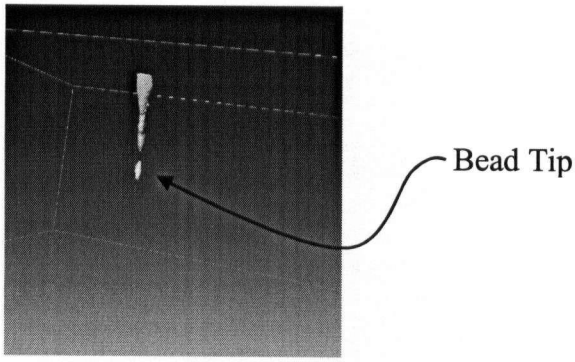

Figure 2 - 9 : Identification of the stylus tip in the ultrasound volume. The isosurface of the volume illustrates the shape of the stylus and the location of the bead at the tip.

Given the positions of the stylus tip in both the volume (${}^{V}x\ {}^{V}y\ {}^{V}z$) and the phantom box coordinate systems (${}^{B}x\ {}^{B}y\ {}^{B}z$), the probe calibration transform ${}^{P}\mathbf{T}_{V}$ can be solved. The location of the stylus tip should satisfy the equation

$$\begin{bmatrix} {}^{B}x \\ {}^{B}y \\ {}^{B}z \\ 1 \end{bmatrix} = {}^{B}\mathbf{T}_{P}\,{}^{P}\mathbf{T}_{V} \begin{bmatrix} {}^{V}x \\ {}^{V}y \\ {}^{V}z \\ 1 \end{bmatrix}. \tag{2-9}$$

As before, ${}^{B}\mathbf{T}_{P}$ is the transformation between the probe and the phantom box coordinate system and its value is directly measured by the Optotrak. The top three components of the equation give three equations to solve the six unknown parameters in ${}^{P}\mathbf{T}_{V}$. A minimum of six equations from three pairs of position coordinates is needed. In this study, five pairs of position coordinates are chosen to create fifteen equations. Unlike the other methods, more than one ultrasound volume is needed here. With the 15 nonlinear equations, the six parameters of ${}^{P}\mathbf{T}_{V}$ are solved using the Powell dogleg optimization algorithm.

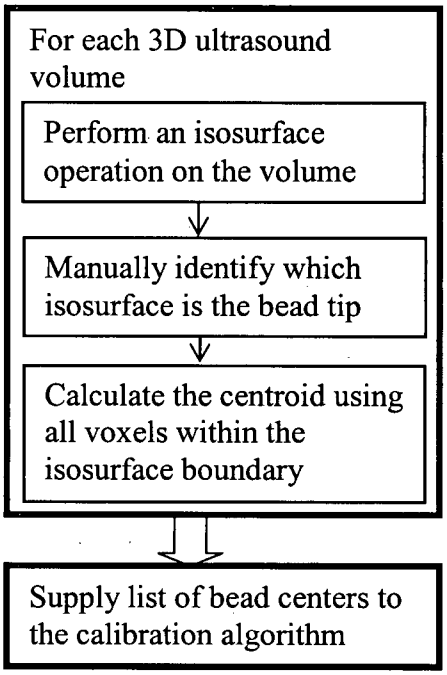

Figure 2 - 10 : The segmentation procedure to identify the center of the bead tip in the ultrasound volume.

2.4 Verification

The calibration solutions of the three methods are verified in terms of reproducibility, accuracy of a known position and reconstruction accuracy of distances between two fixed points from two volumes.

2.4.1 Calibration Reproducibility Tests

The reproducibility of the three calibration methods is assessed by evaluating their stability across multiple trials. The IRLEDs on the ultrasound probe are securely mounted, so their relative positions on the probe are fixed. This indicates that different trials to solve the calibration transformation matrix (${}^{P}\mathbf{T}_{V}$) should ideally yield the same result. However, errors in calibration cause slightly different results for each calibration trial. Two metrics are computed to evaluate reproducibility. The first metric is the standard deviation of the six parameters measured over all trials. To analyze the effect of

reproducibility on the location of a voxel in space, a second metric measures the variation in position of the furthest corner (${}^{V}x_{MAX}$, ${}^{V}y_{MAX}$ ${}^{V}z_{MAX}$) in the ultrasound volume, given the variations in the calibration parameters. The difference in position between a pair of calibration trials $({}^{P}\mathbf{T}_{V})_1$ and $({}^{P}\mathbf{T}_{V})_2$ is

$$\Delta\,{}^{P}\underline{\mathbf{x}} = ({}^{P}\mathbf{T}_{V})_1\,{}^{V}\underline{\mathbf{x}}_{MAX} - ({}^{P}\mathbf{T}_{V})_2\,{}^{V}\underline{\mathbf{x}}_{MAX} \tag{2-10}$$

where

$${}^{V}\underline{\mathbf{x}}_{MAX} = \begin{bmatrix} {}^{V}x_{MAX} \\ {}^{V}y_{MAX} \\ {}^{V}z_{MAX} \\ 1 \end{bmatrix}. \tag{2-11}$$

This measure computes the variation of the transformed position (in the probe coordinate system). The vector ${}^{V}\underline{\mathbf{x}}_{MAX}$ is constant among all pairs of calibration matrices from all trials. In each method, 45 values of $|\Delta\,{}^{P}\underline{\mathbf{x}}|$ are computed from pairs of calibration solutions.

To ensure that all trials are independent in volume acquisition, the ultrasound probe is positioned at different positions and orientations relative to the phantom in the IXI-wire and the cube methods. In the stylus method, the stylus is located at different locations. Table 2-1 illustrates the ranges of the variations in the scanning pattern of the probe for the IXI-wire and the cube methods and also shows the variation in the position of the bead tip for the stylus methods.

Table 2 - 1 : Ranges of variation in the scanning pattern or the bead tip position.

	Scanning Pattern, ${}^{B}\mathbf{T}_{P}$		Bead Tip Position
	Cross-Wire	Cube	Stylus
x translation (mm)	8.0	28.8	36.7
y translation (mm)	10.9	1.1	35.9
z translation (mm)	64.1	16.6	48.2
α rotation around z-axis (degree)	12.0	5.3	n/a
β rotation around y-axis (degree)	7.9	16.8	n/a
γ rotation around x-axis (degree)	2.4	1.5	n/a

2.4.2 Point Accuracy Tests

The point accuracy of the calibration solutions is assessed by scanning the stylus over 10 different positions. Here, the ultrasound probe is held stationary and the stylus is moved. The global position (in the phantom box coordinate system) of the bead tip is measured by the Optotrak and its position in the ultrasound volumes is also identified by the segmentation and centroid algorithms described in the stylus method. Provided that there is a perfect calibration solution, the global position of the bead tip transformed from its volume position should match the position measured by the Optotrak. The difference between these two positions is

$$\Delta\, {}^{B}\underline{\mathbf{x}}_{ij} = ({}^{B}\mathbf{T}_{P})_{i}\,({}^{P}\mathbf{T}_{V})_{j}\,{}^{V}\underline{\mathbf{x}}_{i} - ({}^{B}\underline{\mathbf{x}}^{Optotrak})_{i} \tag{2-12}$$

where

$${}^{V}\underline{\mathbf{x}}_{i} = \begin{bmatrix} {}^{V}x_{i} \\ {}^{V}y_{i} \\ {}^{V}z_{i} \\ 1 \end{bmatrix}. \tag{2-13}$$

The subscript i represents the 10 sets of measurements of the bead tip in both the ultrasound volume (V) and phantom box (B) coordinate systems. The transformation from the probe to the phantom box coordinate system, ${}^{B}\mathbf{T}_{P}$, is also directly measured by

the Optotrak. The subscript j represents the index of the calibration solutions in each method.

This test measures the difference between the true position of a point in space and the location of the point measured by the calibrated ultrasound probe. The tip of the stylus can be considered as the true position in space, because it is known to within 0.23 mm, as stated earlier. The errors from calibration are an order of magnitude larger.

The results are repeated for the 10 calibration matrices derived in the calibration reproducibility tests. In this way 100, values of $|\Delta^{B}\underline{\mathbf{x}}|$ are computed for each method. The ranges of stylus positions are 28.7 mm in x, 20.0 mm in y and 56.3 mm in z.

2.4.3 Reconstruction Accuracy Tests by Distance Measurement

The reconstruction accuracy is evaluated by scanning the four-pin device shown in Fig. 2-11. The device consists of four pins arranged at the corners of a flat board. The head of each pin is a 3 mm sphere. The actual distances of the diagonals and the top and bottom lengths are measured with a caliper. The distance of the diagonal is 102.52 ± 0.03 mm and the length is 100.44 ± 0.03 mm. Ten ultrasound volumes are then acquired of the left pins and another 10, for the right pins, for a total of 20 volumes. Each volume only contains either the two left or the two right pins. In each ultrasound volume the bead heads are segmented, producing a pair of point measurements in space. Using the calibration matrices and the Optotrak measurements of the ultrasound probe, the distances between the left and the right pins are compared with the actual distances. The metric for accuracy is simply the difference between the measured and the actual distances. The measured distance is expressed as:

$$\text{Measured Distance} = \sqrt{(\Delta d)^{T}(\Delta d)} \qquad (2\text{-}14)$$

where

$$\Delta d = {}^{B}(\mathbf{T_L})_P \, {}^{P}\mathbf{T}_V \begin{bmatrix} {}^{V}x_L \\ {}^{V}y_L \\ {}^{V}z_L \\ 1 \end{bmatrix} - {}^{B}(\mathbf{T_R})_P \, {}^{P}\mathbf{T}_V \begin{bmatrix} {}^{V}x_R \\ {}^{V}y_R \\ {}^{V}z_R \\ 1 \end{bmatrix}. \qquad (2\text{-}15)$$

$[{}^{V}x_L \; {}^{V}y_L \; {}^{V}z_L \; 1]^T$ and $[{}^{V}x_R \; {}^{V}y_R \; {}^{V}z_R \; 1]^T$ are the positions of the pin heads in the left and right volumes, respectively. The pair of the left and right volumes produce four distances, as indicated in Fig. 2-11. Ten volumes from each side create 100 pairs of possible combinations and each pair produces four distances. Again, the 10 calibration results from the calibration reproducibility tests are used giving a total of 4000 accuracy values for each calibration method.

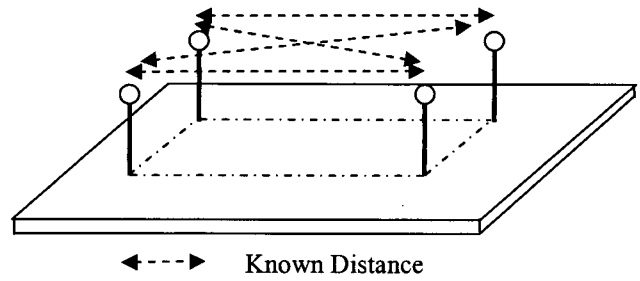

Figure 2 - 11 : The four-pin device for evaluation of accuracy. The dashed arrows represent the measured distances between the left beads and the right beads.

To ensure independence among the trials, each ultrasound volume is taken at a unique location. The ranges of translation in the left volumes are 29.7 mm in x, 0.3 mm in y and 7.7 mm in z, whereas the ranges of rotation are 96.0 ° in α, 4.6 ° in β and 96.1 ° in γ. The ranges of translation in the right volumes are 38.2 mm in x, 3.2 mm in y and 15.5 mm in z, whereas the ranges of rotation are 89.9 ° in α, 5.5 ° in β and 94.0 ° in γ.

2.5 Results

Table 2-2 lists the means and standard deviations of the solutions for each method, in terms of the six translation and rotation parameters. The standard deviation is a measure of the reproducibility of the calibration method. Table 2-3 lists the calibration reproducibility results using the metric based on variation in voxel position. Table 2-4 lists the results of the point accuracy tests. Note that RMS error is calculated in 3D as

$$\text{RMS error} = \sqrt{(\text{RMS error\_x})^2 + (\text{RMS error\_y})^2 + (\text{RMS error\_z})^2} \,. \tag{2-16}$$

Table 2-5 lists the result of the reconstruction accuracy tests.

Table 2 - 2 : Calibration results. Standard deviation is calculated over ten trials for each method.

	IXI-Wire		Cube		Stylus	
	Mean	Std. Dev.	Mean	Std. Dev.	Mean	Std. Dev.
x translation (mm)	-4.05	0.26	-4.76	0.45	-3.39	1.11
y translation (mm)	203.15	0.20	205.08	0.82	203.24	1.80
z translation (mm)	-63.13	0.84	-63.04	0.81	-64.97	2.62
α rotation around z-axis (deg)	-3.28	0.18	-2.24	0.70	-2.91	1.25
β rotation around y-axis (deg)	0.07	0.64	-2.17	0.29	-1.82	2.20
γ rotation around x-axis (deg)	3.98	0.28	3.86	0.84	3.71	3.77

Table 2 - 3 : Calibration reproducibility results. This test measures the variation of distance for the most distant voxel in the ultrasound volume over the ten trials for each calibration method.

	IXI-wire	Cube	Stylus
No. observations	45	45	45
Max (mm)	3.63	2.35	9.73
Mean (mm)	1.50	1.16	5.13
Std. dev. (mm)	0.84	0.54	2.47

Table 2 - 4 : Point accuracy results. This test measures the relative error in localizing a known point in space.

	IXI-wire	Cube	Stylus
No. observations	100	100	100
Max error (mm)	3.78	6.25	4.68
RMS error (mm)	2.15	4.91	2.36

Table 2 - 5 : Reconstruction accuracy results. This test measures the error in measuring the distance between two known points in space.

	IXI-wire	Cube	Stylus
No. observations	4000	4000	4000
Max error (mm)	2.56	2.67	3.71
RMS error (mm)	1.52	1.59	1.85

2.6 Discussion

To identify the sources of errors in the calibration methods, it is useful to consider eqn (2-5) for the IXI-wire method, eqn (2-8) for the cube method and eqn (2-9), for the stylus method. Based on the transformation matrices from the equations, the sources of errors are:

- Optical tracking system. Errors from the Optotrak affect the measurements of the stylus and the ultrasound probe relative to the phantom box (e.g., ${}^{B}\mathbf{T}_{P}$). All three calibration methods are therefore affected by errors in the Optotrak.
- Calibration of the stylus. As previously mentioned, the stylus is used both as a phantom and as a position-measuring tool. In both cases, the position of the tip is calculated from the IRLEDs on the stylus. Any error in measuring tip location with respect to the Optotrak affects all three calibration methods. In the IXI-wire method, the stylus is used to measure the wire positions when creating the reference data set. An error in the reference structure will affect ${}^{B}\mathbf{T}_{V}$, because it is based on the registration of the ultrasound volume to the reference structure. In the cube method, the positions of the three cube faces are measured with the stylus to determine the transformation between the cube (C) and phantom box (B) coordinate system, ${}^{C}\mathbf{T}_{B}$. In the stylus method, the stylus is used directly in calibration.
- Speed of sound. A small error exists because the speed of sound in water at 37°C (1523.6 m/s (Bilaniuk and Wong 1993)) may not match the speed of sound used by the ultrasound machine to convert time into distance. Using a higher temperature or different fluids is not recommended by the manufacturer. If 1540m/s was the speed assumed by the manufacturer, the mismatch would produce a theoretical position error of 1.06%.
- Feature identification in the ultrasound volumes. In the IXI-wire method, the registration of the ultrasound volume (V) in the phantom box (B) coordinate system is used to compute ${}^{B}\mathbf{T}_{V}$. The registration contains errors from uncertainty in the depiction of the wires. The wires appear with finite and slightly nonuniform thickness, so the center of the wire is not perfectly known. In the cube method, the

planes are depicted as bright reflections, with some reverberation and blurring. The edge of the plane does not appear as a perfect step, so there is uncertainty in the location of the true edge. In the stylus method, the center of the bead tip appears as a bright dot that is often nonsymmetric. The center of the bead is estimated from the centroid of the isosurface. The intensities are not perfectly uniform around the bead center, since ultrasound reflects more strongly from the top of the bead, so there is uncertainty in whether the centroid corresponds to the true center of the bead.

The source of error from the Optotrak is small. The manufacturer reports an accuracy of measuring the IRLED position as 0.15 mm and this was verified in an independent test (Rohling et al. 1995). In comparison with the errors from the calibration reproducibility, point accuracy and reconstruction accuracy tests, the Optotrak error is insignificant. The source of error from stylus calibration is 0.12 mm for the sharp tip and 0.23 mm for the bead. These errors are also small in comparison with the test results. To test the speed of sound error, the IXI-wire phantom at 37°C produced a 0.43 mm RMS error in the distances between the two levels of wires. For comparison, a sealed commercial quality-assurance phantom (Model 040, CIRS, VA, USA) with a verified speed of sound of 1540 m/s produced 0.17 mm RMS error in axial distance measurements between wires. So the error from speed of sound is significant but small. It is believed that the majority of errors in each calibration method do not come from the measurement tools, but come from the feature identification step. The typically grainy appearance (speckle) of the features in the ultrasound volumes is the primary source of errors because it is difficult to find their true positions in the volumes.

According to the calibration reproducibility results in Tables 2 and 3, the IXI-wire and cube methods appear to be more stable than the stylus method. A possible explanation for the worse reproducibility of the stylus method is uncertainty in measuring the bead's position in the ultrasound volume. Since the ultrasound reflects most strongly from the top surface of the bead, the largest possible error would be equal to the radius of the sphere (all reflection from the top surface). The diameter of the bead is 3.0 mm, so the error is, at worst, 1.5 mm. The wires in the IXI-wire phantom are thinner and less reflective, so they appear as more uniform dots. The faces of the cube phantom appear as

flat planes. The uncertainty with the planes lies mainly in measuring where the true cube face starts, not the orientation of the face.

To assess the correctness of the calibration solutions, the point accuracy tests match the position of the stylus tip to the dot depicted in the ultrasound volume. Table 4 shows that the IXI-wire method performed best. Although the stylus method is less repeatable than the cube method, it has a better point accuracy than the cube method. One possible explanation is that the errors from identifying the bead center in calibration are partly offset with identifying the bead center in the point accuracy tests (although the tests were independent). Another possible explanation is that the cube method simply found a repeatable, but slightly wrong, calibration. Since the cube phantom is aluminum, the ultrasound reflects almost completely off the face. The edge detector identifies the plane face wherever the slope of the echo magnitude reaches a maximum. In other words, it measures the location of the sharpest transition from dark to light. But this may not correspond to the true location of the plane if there is nonlinear interaction between the pulse and the plane. So it is feasible to get repeatable but incorrect measurements of plane position.

In the reconstruction accuracy tests by distance measurement, the stylus method is less accurate and the IXI-wire method again shows the best results. Previous papers have reported overall point accuracy for 3D probe calibration of 2.0-2.2 mm (Lange and Eulenstein, 2002) and 1.1 mm (Bouchet, et al. 2001). The accuracy numbers in Table 4 show comparable results. However, comparing the performance of the calibration methods in this paper with the results from other research groups should be done with extreme caution. The previous work did not address reconstruction accuracy by distance measurement and used different methods and different amount of test data to quantify calibration reproducibility and point accuracy measurements. Moreover, comparisons should only be made for tests done under similar conditions, including the test protocol, the phantoms construction, the tracking system, the 3D ultrasound system and the amount of data used in the evaluation.

A previous paper has also compared the use of points, lines and planes for calibration of 2D probes (Prager, et al. 1998). In that study, the use of planes produced straight-line features in the image that provide redundant information for feature

extraction. The large amount of redundant data helped to reduce the influence of random measurement errors. In the current study of 3D probes, both the wire and cube methods contain redundant features in the ultrasound volume. In other words, only a small portion of the wires and planes are theoretically needed to solve the calibration, but the redundant features help to reduce the influence of noise.

The calibrations produced by the cube method are not as good as those by the IXI-wire method. There is uncertainty in determining the cube surface voxels, which leads to relatively poor point accuracy (Table 2-4). The ultrasound volume that depicts the cube surface contains reverberation artifacts because the cube is a strong reflector of ultrasound energy. When the edge detector is then applied to identify the surface voxels according to the gradient, the reverberations may affect the location of the maximum gradient. This, in turn, can produce systematic errors that are difficult to correct. The errors in identifying the features with the IXI-wire method are more random in nature.

A final question to consider is which method is the most efficient one. One factor is the ease of use for each method. The positions of the cube and the IXI-wires need to be known relative to the box. The stylus tip also needs to be known relative to the IRLEDs on the shaft. All of these measurements can be performed once, at the time of device construction. They do not need to be repeated, as long as the devices are stable and rigid. These measurements, therefore, do not contribute much to the ease of use. The IXI-wire and the cube methods have an advantage over the stylus method, because only a single ultrasound volume is needed for calibration. The IXI-wire method does not need any additional feature extraction step before solving the calibration. The original ultrasound data are used in the registration with the reference volume. The reference volume only needs to be created once, at the time of phantom construction. The cube and the stylus methods require an algorithm to semiautomatically identify the features in the ultrasound volume. So, given a previously-constructed phantom and reference volume, the IXI-wire method appears easiest to use.

The time needed to perform calibration is another factor for efficiency. It depends on three steps: phantom construction, data acquisition and analysis. The cube and stylus phantoms are relatively easy to construct. The IXI-wire phantom requires the wire locations to be accurately measured – a process that takes approximately 5 minutes. A

similar time is needed to measure the cube faces. Given solid construction of all of the phantoms, no additional set-up time is needed for each calibration. Thereafter, the calibration times depend mainly on the data analysis step because of the need for manual interaction. The stylus method requires the largest amount of time because identifying the bead position in a single volume includes a manual step. The manual identification must be repeated for all volumes. The total time required to perform one calibration using the stylus method with 15 equations is approximately one hour. The cube method only requires one volume for calibration and requires manual identification of regions with large reverberation effects. The time required to perform calibration with the cube is approximately thirty minutes. The IXI-wire method only requires one volume for calibration and only the initial guess of the registration is required by the user. In practice, the initial guess can be provided automatically since the probe is always placed on the top side of the phantom, so its approximate location can be used as the initial guess. The time required to perform one calibration with the IXI-wire method is approximately twenty minutes.

2.7 Conclusion

In this study, three calibration methods were developed for determining the coordinate transformation between the ultrasound volume and the position tracking sensor attached to the ultrasound probe. Although wires and planes have been used previously in 2D calibration, the cube and the IXI-wire methods are both new methods. Each calibration method used a unique set of geometric properties to establish the equations for calibration. It was shown that the calibration equations could all be based on a set of rigid body transformations. The key to all of the techniques was to match correctly the features of the phantom in both the ultrasound volume and their true location in space. The performance of the methods is determined mainly by the clarity of the features depicted in the ultrasound volume.

Performance was measured in terms of calibration reproducibility, point accuracy and reconstruction accuracy by distance measurement. The best overall performance was achieved with the IXI-wire method. The IXI-wire technique registered a single ultrasound

volume of the wires to a reference volume containing a geometric description of the wires. The thin wires appeared as relatively clear dots that minimized uncertainty in the location of the wires. The cube and stylus methods also gave good performance, but more care is needed in feature extraction. All three methods have a level of accuracy similar to the accuracy reported in previous studies on 3D probe calibration. This gives confidence in the use of these calibration methods in image-guided procedures.

Chapter 3 Extended Field-of-View

This study proposes to develop a novel system that registers a series of individual volumes to produce a 3D extended view. The challenge is to stitch together the individual volumes in the presence of errors from calibration, speed of sound variations, refraction, patient motion, and other errors. The system meets the challenge with the use of block-based registration methods. The starting point for registration is the position of the probe, measured by a tracking system for every individual volume.

The objectives of this study are 1) demonstrate a proof-of-concept of 3D extended field-of-view with experiments *in vitro* and *in vivo*, 2) evaluate the reconstruction reproducibility among extended volumes of the same region, 3) evaluate the improvement of alignment by the registration methods and 4) evaluate the reconstruction accuracy by distance measurements of a known length.

3.1 Acquisition and Processing Systems

The acquisition system consists of a 3D ultrasound scanner (Voluson 730 Pro) and an optical tracking system with 0.15 mm RMS accuracy (Optotrak 3020). It is identical to that in the calibration study (Section 2.3, Figure 2-1). Ultrasound volumes are transferred from the Voluson to the computer using a proprietary software package from GE Medical Systems called 3DView2000. 3DView2000 uses the DICOM (Digital Imaging and Communications in Medicine) standard.

The acquisition rate of the ultrasound volumes with a 14.4 cm depth and a 75° sweep is 0.9 Hz. This rate represents a tradeoff among depth, sweep angle and image quality; the largest volume and best quality were chosen here. At this rate, continuous movement of the probe during acquisition would result in distortions and streaky features in the volumes. Therefore, our 3D extended field-of-view system utilizes a "hold-and-shoot" scanning protocol that keeps the probe stationary for each acquisition of a static volume. A set of such static volumes comprises an extended volume.

The position tracker measures the position and orientation of the probe IRLEDs placed on the handle. A preliminary set-up procedure is performed to define a coordinate

system (origin and axes) based on the IRLEDs. There are eight IRLEDs fixed rigidly on the two sides of the ultrasound probe, with four IRLEDs on each side. Because the cameras on the tracking system must view only three or more IRLEDs to compute a valid measurement, this configuration allows the probe to be tracked at any orientation. The IRLED position measurements must be converted into measurements of the coordinate system of the ultrasound volumes. This is done using a fixed spatial coordinate transformation determined by calibration (see Chapter 2).

The overlapping regions of the set of acquired volumes are the subject of registration for accurate alignment. The spatial measurements of the volumes by the position tracker provide the initial guess for the registration procedure. Volume registration differs from image registration of 2D extended field-of-view in terms of the degrees of freedom. Volume registration determines six degrees of freedom (three for translation and three for rotation), whereas image registration determines three degrees of freedom (two for translation and one for rotation). Most of the commercial 2D extended field-of-view systems do not use a position tracker, but instead perform registration in real-time based solely on image content. This is feasible in 2D since the search space of registration is smaller, the size of the overlapping regions is relatively large, and the high frame rate means subsequent images contain similar features. For the 3D case using hold-and-shoot acquisition, the size of the overlapping regions can vary greatly and the registration search space is much larger. This project also proposes to use block-based registration with warping, which adds additional complexity to the search space.

The use of registration with warping addresses the issue of image distortion inherent from refraction and speed-of-sound errors with ultrasound. These errors displace the structures both laterally and axially from their correct locations (Kremkau 2002). The block-based registration method only applies to the overlapping regions for the purpose of creating a panoramic view, although a similar technique has been applied previously to entire images for spatial compounding (Groves and Rohling 2004). In spatial compounding, multiple images of the same region are taken from different viewpoints and then registered for best alignment before compounding together. The same issues of image distortion due to speed-of-sound variations and refraction apply here.

The warping and registration programs were implemented in Visual C++ and compiled to run on an Itanium 64-bit workstation (Intel Corporation, Santa Clara, CA, USA). The high-performance Itanium workstation is needed to meet the computational needs of the registration algorithm. The workstation has a 1.0 GHz Itanium 2 processor with a 1.5 MB cache of on-chip memory. It also contains 4.0 GB of on-board RAM (random access memory) to satisfy the demanding memory requirements for volume registration. Unlike conventional 32-bit processors, this memory can be increased for larger studies, although not needed here.

3.2 Implementation

In order to synchronize the ultrasound acquisition and position measurements, we developed a trigger application running on the host workstation of the Optotrak. The trigger uses the serial port of the workstation to emulate the external foot pedal of the Voluson that normally starts ultrasound capture. In this way, a single keystroke on the workstation triggers both the Optotrak and the Voluson simultaneously.

3.3 Reconstruction Methods

The main steps of the reconstruction methods are alignment of the individual volumes and combining the results into a common coordinate system. The alignment can be based on the position tracker measurements or include image-based registration to further align the features. The data is combined by interpolation and compounding (averaging the pixel values together). Linear interpolation was implemented using the source code published by Press et al. (1992).

Two new visualization applications were developed with the use of the Visualization Toolkit (Kitware, Inc., Clifton Park, NY, USA) for viewing the extended fields of view and for verification of the alignment. In this study, three different reconstruction methods were explored: simple compounding without registration, block-based warping registration, and block-based rigid-body registration.

3.3.1 Simple Compounding Without Registration

Simple compounding is the easiest technique and uses only the position tracker measurements to align the individual volumes. Each volume is transformed into a common space using two transformation matrices, ${}^{C}\mathbf{T}_{P}$ and ${}^{P}\mathbf{T}_{V}$. ${}^{P}\mathbf{T}_{V}$ is the transformation between the coordinate systems of the ultrasound volume (V) and the probe (P). ${}^{C}\mathbf{T}_{P}$ is the transformation between the coordinate systems of the probe (P) and the common space (C). ${}^{P}\mathbf{T}_{V}$ is determined *a priori* by calibration and remains fixed for all acquired volumes since the IRLEDs are fixed on the probe and the settings of the Voluson (depth and sweep angle) are unchanged during acquisition. The IXI-wire calibration method was chosen here because it can be used with the 3D probe and was shown to provide a relatively accurate result with 2.15 mm RMS error (Chapter 2). ${}^{C}\mathbf{T}_{P}$ is the spatial measurement of the probe position by the Optotrak and is different for each acquired volume. The equation to transform a voxel in one volume into the common space is:

$$ {}^{C}\underline{\mathbf{x}} = {}^{C}\mathbf{T}_{P}\,{}^{P}\mathbf{T}_{V}\,{}^{V}\underline{\mathbf{x}} \tag{3-1} $$

where

$$ {}^{V}\underline{\mathbf{x}} = \begin{bmatrix} {}^{V}x \\ {}^{V}y \\ {}^{V}z \\ 1 \end{bmatrix}, \qquad {}^{C}\underline{\mathbf{x}} = \begin{bmatrix} {}^{C}x \\ {}^{C}y \\ {}^{C}z \\ 1 \end{bmatrix}. \tag{3-2} $$

The multiplication of these two matrices (${}^{C}\mathbf{T}_{P} \cdot {}^{P}\mathbf{T}_{V}$) is ${}^{C}\mathbf{T}_{V}$, which represents the transformation of a voxel to its position in the common space. Errors in ${}^{C}\mathbf{T}_{V}$ can arise from refraction, speed of sound variations and inaccurate probe-sensor calibration. The errors will produce small misalignment of the image features among neighbouring volumes. Two new reconstruction methods using image-based registration are explored to correct this misalignment. ${}^{C}\mathbf{T}_{V}$, as described, is used in the following methods as an initial guess for the registration.

3.3.2 Block-based warping registration

The block-based warping algorithm was inspired by Krücker et al. (2002) and Ourselin et al. (2000). Krücker et al. (2002) applied the technique to improve spatial resolution specific to ultrasound volume spatial compounding. We use a similar approach here on the overlapping regions among volumes. The objective of the algorithm is to determine the elastic registration transformation between two ultrasound volumes. One is considered as the reference volume, V_{ref}, and the other is the adjacent volume, V_{adj}, overlapping with the reference volume. The algorithm is an iterative process to register a series of volumes together. The first acquired volume becomes the initial V_{ref} and the next adjacent volume is V_{adj}. Once they are reconstructed by elastically registering V_{adj} into V_{ref}, and interpolating together, this intermediate panoramic result becomes V_{ref} for the next adjacent volume. This process continues until the last volume is acquired. The basic principles of the elastic registration are to divide the overlapping region of V_{adj} into smaller blocks, then match each block to V_{ref} by searching for the best position and orientation that maximizes a similarity measure. In this application, a six-dimensional search space (three translations and three rotations) is searched to find the maximum correlation coefficient for each block (Appendix B). An overview of the entire algorithm is illustrated in Fig. 3-1.

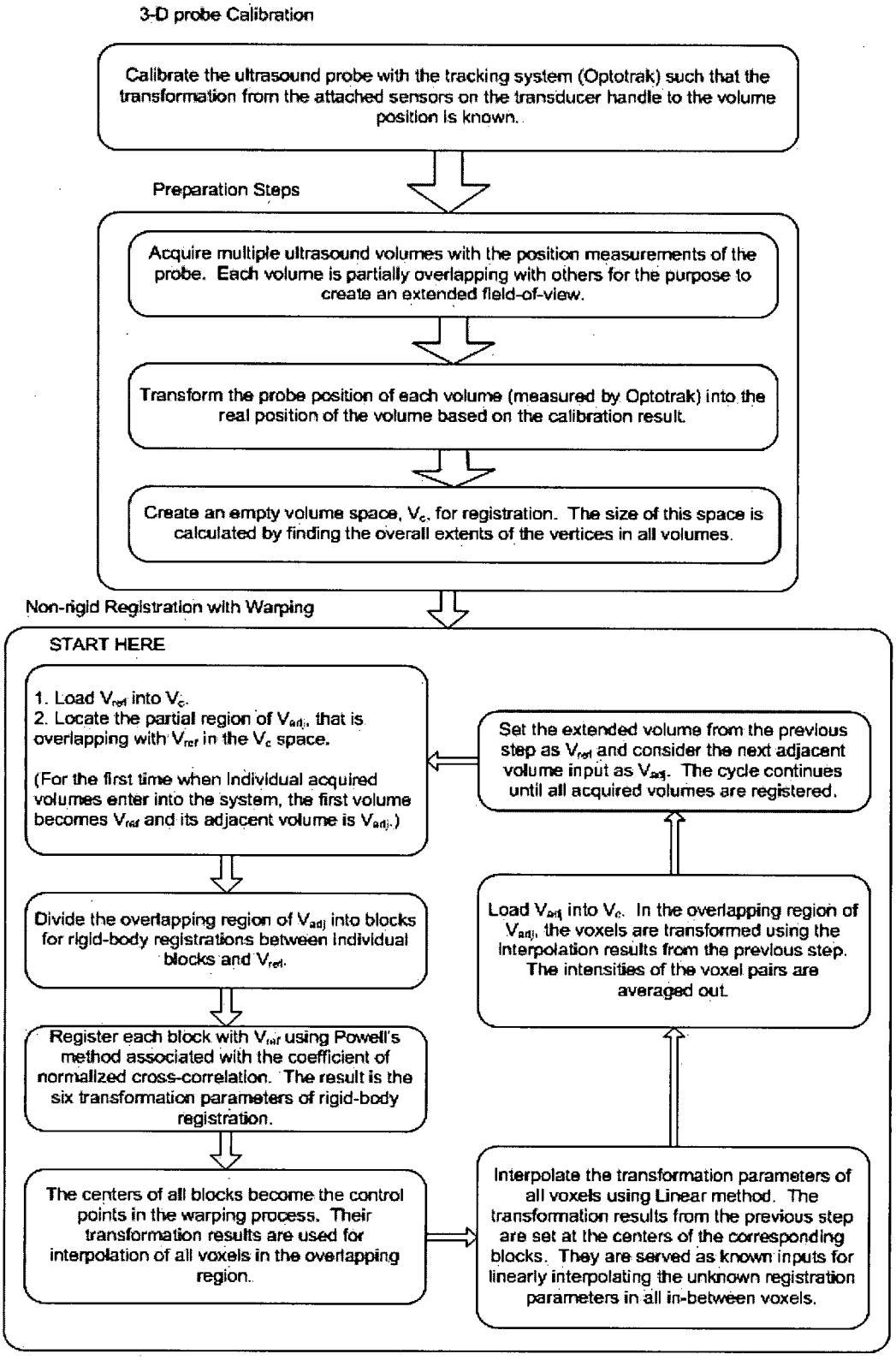

Figure 3 - 1 : The Flow diagram of the extended field-of-view reconstruction method using block-based warping.

Each of the small blocks is registered independently, so each will produce a different registration. The position and orientation of the registered blocks become the control points. The set of control points therefore define the warping of V_{adj}. Also, each of the blocks is deformed before compounding with V_{ref}. This is done by interpolating (Appendix C) the nearby control points around each voxel in every block (Parent 2002). So every voxel has a different spatial transformation to the common coordinate system. This means the blocks are deformed prior to compounding with V_{ref}.

The three translations (x, y, z) and three orientation angles (α, β, γ) of the registration can be described by a single homogenous transformation matrix (Appendix A)

$$\begin{bmatrix} \cos\alpha\cos\beta & \cos\alpha\sin\beta\sin\gamma - \sin\alpha\cos\gamma & \cos\alpha\sin\beta\cos\gamma + \sin\alpha\sin\gamma & x \\ \sin\alpha\cos\beta & \sin\alpha\sin\beta\sin\gamma - \cos\alpha\cos\gamma & \sin\alpha\sin\beta\cos\gamma - \cos\alpha\sin\gamma & y \\ -\sin\beta & \cos\beta\sin\gamma & \cos\beta\cos\gamma & z \\ 0 & 0 & 0 & 1 \end{bmatrix} \tag{3-3}$$

that is multiplied by ${}^{C}\underline{\mathbf{x}}$ to obtain the registered location (Sciavicco and Siciliano, 1996). So for the first step of block-based registration (search for peak correlation coefficient), each voxel in a block of V_{adj} will use the same transformation matrix. After registration (compounding with V_{ref}), each voxel will use a different matrix using the interpolated translations and orientations.

The dimensions of each block are 55x55x55 voxels corresponding to 39.6 mm x 39.6 mm x 39.6 mm. These dimensions were chosen so that each block contains some significant features for matching. The iterative search method to find the peak correlation coefficient (Appendix B) for each block was implemented using Powell's method (Press et al. 1992). Details of Powell's method are given in Appendix D. Maximum allowable values for the position and orientation were also set to limit the size of the search space. Every block cannot translate over 7 mm and cannot rotate more than 5° with respect to the position tracker measurements. These two search limits were found experimentally and accommodate the maximum errors with our system. A wider range is possible but there is a tradeoff with speed.

3.3.3 Block-based rigid-body registration

A third method is a variation of block-based warping registration. The difference is that the block-based rigid-body registration does not perform the interpolations of voxels in each block and displaces each block as a whole. This method does not require interpolation so after registration every voxel within a block is transformed with the same matrix. This improves the speed of the calculations but is a simpler registration method.

3.4 Experiments

For the study performed *in vitro*, volumes were acquired from a fetus phantom (CIRS, Inc., Norfolk, VI, USA). The external dimensions of the phantom are 40.6 x 22.9 x 22.9 cm. All ultrasound volumes were taken with a depth setting of 14.4 cm and a 75° sweep angle. This corresponds to a volume of 171 x 159 x 165 square voxels 0.72mm in size, or 12.3 x 11.4 x 11.9 cm. Six volumes are needed to reconstruct the whole fetus in a single extended field of view.

For the study performed *in vivo*, scans were performed of the abdominal blood vessels (aorta and vena cava), the liver, and kidneys of a healthy human subject. The acquisition settings of the ultrasound volumes were identical to the phantom study. The subject was requested to lie motionless on a bed and to breathe lightly to minimize motion-induced errors during acquisition. In the case of the blood vessels, the objective is to depict the extended tubular shape of the aorta, surrounding structures of the aorta, the vena cava and the associated vascular branches across the abdomen. In the case of the liver, the objective is simply to depict the whole organ and its spatial relationship with its surrounding organs. In the case of the kidney, both kidneys are depicted in a single panoramic view. In these examinations, each extended volume comprises three to eight volumes.

The size of the overlapping regions is an important factor in registration. The region must be large enough to contain sufficient features for accurate registration and

smooth transitions in the extended field of view. In these studies, the overlapping region occupies approximately 20 - 40% of the size of each volume.

The success of the reconstruction was evaluated according to the degree of reproducibility, the improvement in registration, and the accuracy of geometric measurement. The tests on the phantom were repeated ten times. The abdominal vessels were also scanned ten times. Since different scans of the abdomen were also performed (see above), thirty extended field of views covering the blood vessels, the liver and the kidneys were used for the registration improvement tests.

3.5 Verification

3.5.1 Reproducibility

Reproducibility measures the ability to create the same extended field of view of the same region from multiple examinations. Each of the ten extended fields of view should produce similar looking results. The fetus phantom was kept stationary so errors from motion should be small. The human subject also remained approximately still but small random involuntary motions were observed. As mentioned, other possible sources of reproducibility error are refraction, speed-of-sound variations, and probe-sensor miscalibration. The testing of reproducibility aims to investigate the effect of the different registration methods on these errors.

The reproducibility test calculates the normalized cross-correlation coefficient between a pair of extended volumes to evaluate their similarity. Since ten extended volumes are available from both the phantom and human studies, each study gives 45 pairs. This is repeated for all three different reconstruction methods and the correlations coefficients are compared. The correlation coefficient is only calculated for the intersection of a pair of extended volumes to exclude the influence of the black boundary. A higher coefficient indicates a higher reproducibility.

3.5.2 Improvement in registration of overlapping regions

The goal of both block-based warping registration and block-based rigid-body registration is to improve the alignment of the features in the overlapping regions. This is done by calculating a similarity measure, in this case the correlation coefficient. It is expected that an increase in the similarity of the blocks will produce an increase in the similarity of the entire overlapping region. This is measured here by calculating the correlation coefficient of each of the overlapping regions for each of the registration methods. Ten extended volumes of the phantom and thirty extended volumes of the abdomen were used.

3.5.3 Reconstruction accuracy by distance measure

The anatomical geometry should be preserved in an extended field of view if the volumes are accurately reconstructed. The reconstruction accuracy is evaluated by measuring the distance between two easily identifiable features in an extended volume of the fetus phantom. We chose the tip of the nose and the right big toe as the two identifiable points with a known distance. To calculate the distance accuracy, we compared the true distance with the distance measured by an operator on a manually selected reslice of the extended field of view. Again, this was repeated for the ten extended volumes of both studies with all three reconstruction methods.

3.7 Results

Figure 3-2a shows the grouping of the individual volumes of the fetus phantom using the external position measurements. To illustrate an example of the registration of V_{adj} to V_{ref}, we created wire-frame models that outline the blocks in the overlapping region circled in Fig. 3-2a. The different stages of the warping registration are shown in Fig 3-2b to 3-2d. Figure 3-2c can be interpreted as the result of the block-based rigid-body registration or a depiction of the control points for block-based warping registration.

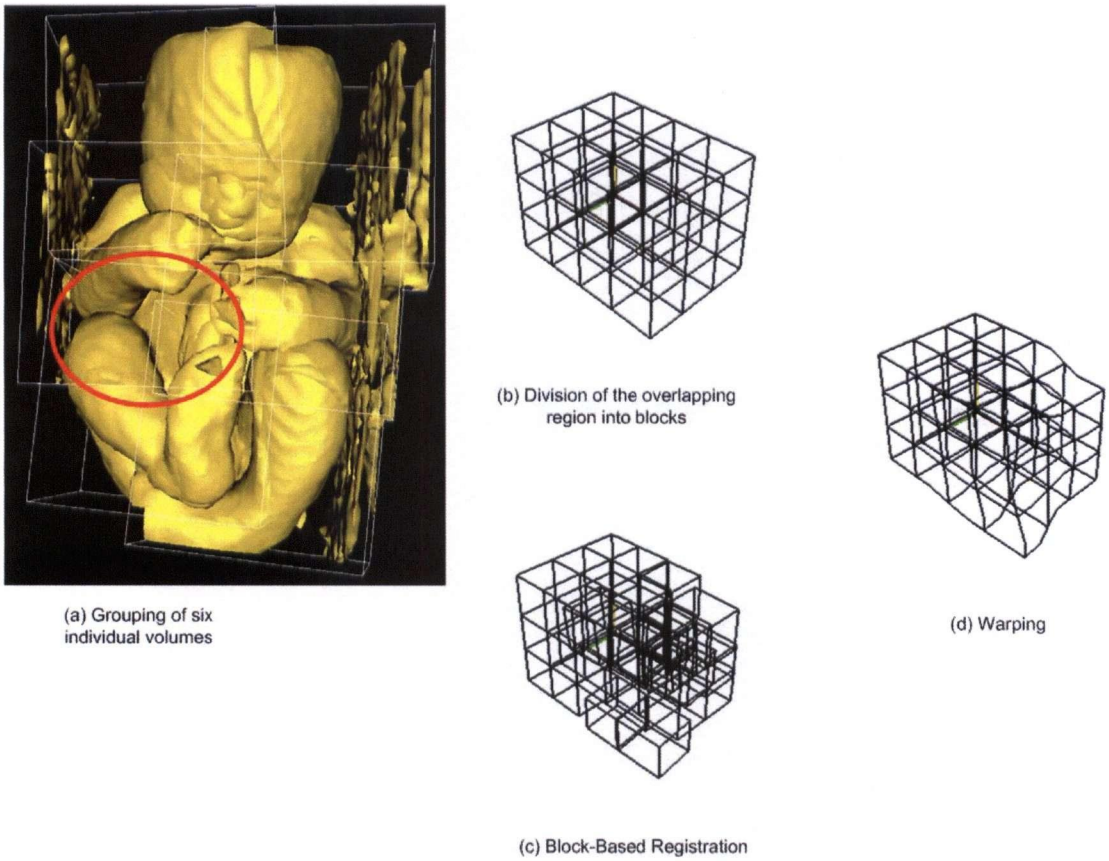

Figure 3 - 2 : Experiments *in vitro*. (a) The set of six individual volumes covering the fetus phantom. Each overlapping region is subject to registration. (b) The overlapping region circled in (a) is divided into smaller blocks. (c) Each block is registered to match its counterpart in the reference volume, V_{ref}, and is displaced accordingly (block-based rigid-body registration). (d) The movement (control points) of the smaller blocks are used to warp the region (block-based warping registration).

Figure 3-3 shows isosurface renderings of the extended volumes produced by the three reconstruction methods. It appears that there is substantial misalignment that remains after reconstruction from either simple compounding or block-based rigid-body registration. This is especially clear in the face of the fetus phantom in Fig. 3-3a and on the right foot and the left leg in Fig. 3-3b. The rendering in Fig. 3-3c from block-based warping registration shows less misalignment.

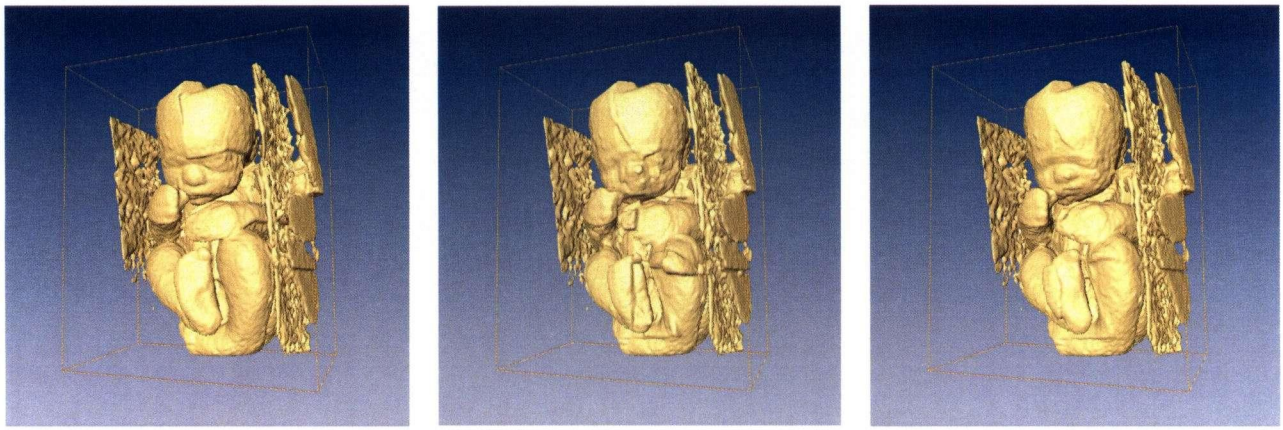

(a) Simple compounding (b) Block-based rigid-body registration (c) Block-based warping registration

Figure 3 - 3 : Experiments *in vitro*. (a) Simple compounding of six individual volumes to reconstruct the fetus phantom. (b) Block-based rigid-body registration of the six volumes. (c) Block-based warping registration of the six volumes. The misalignment of features are evident in the isosurface renderings of (a) and (b) but less evident in (c).

The extended field of view results from the human experiments are shown as multiplanar reslices in Figs. 3-4 to 3-7. These images were created using block-based registration with warping. The liver, kidney and abdominal blood vessels appear clearly in the extended volumes. No obvious signs of misalignment are visible.

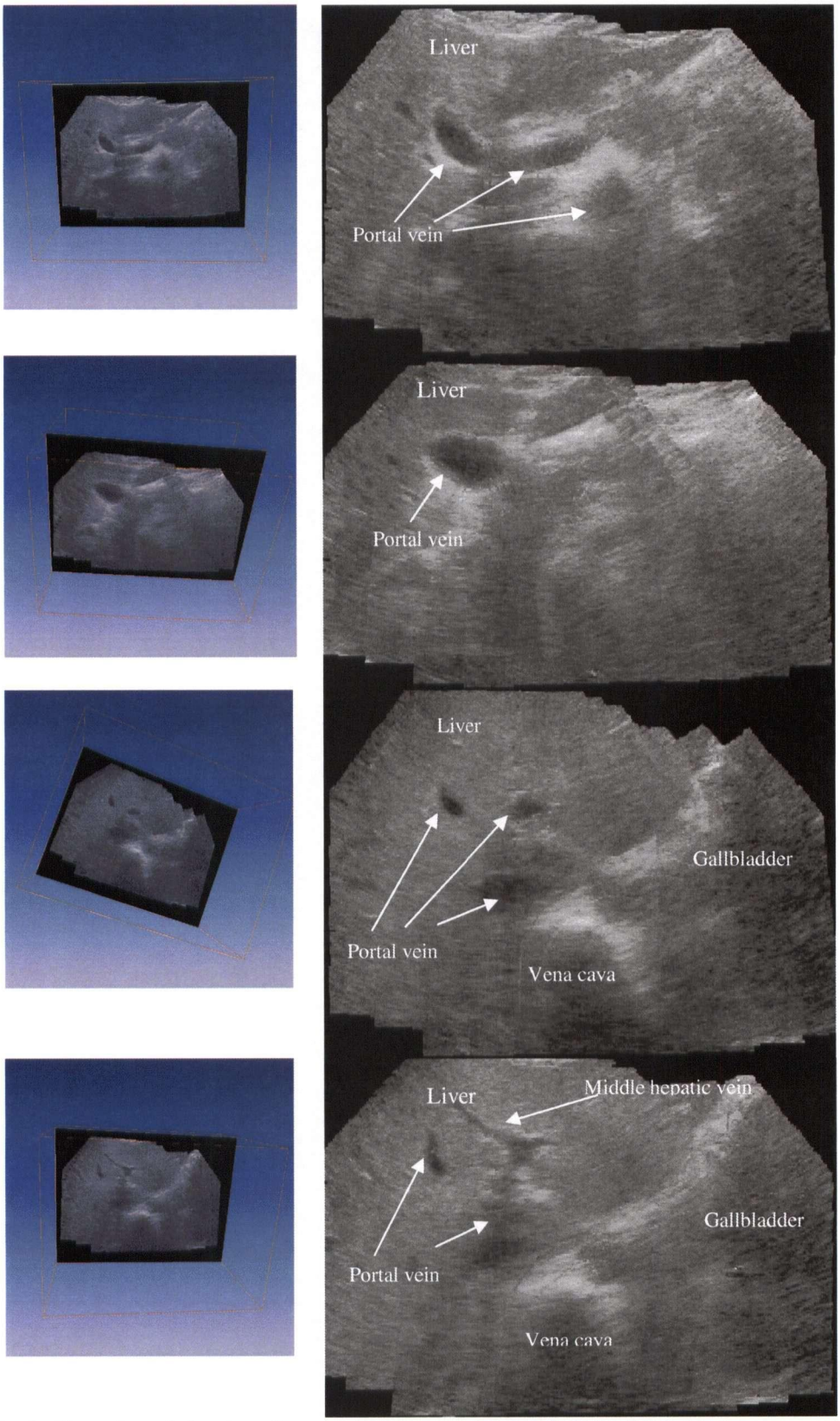

Figure 3 - 4 : Experiments *in vivo*. Four re-slices are extracted from a single *in vivo* extended volume (left) to illustrate the anatomy of the liver. (Block-based warping registration was used.)

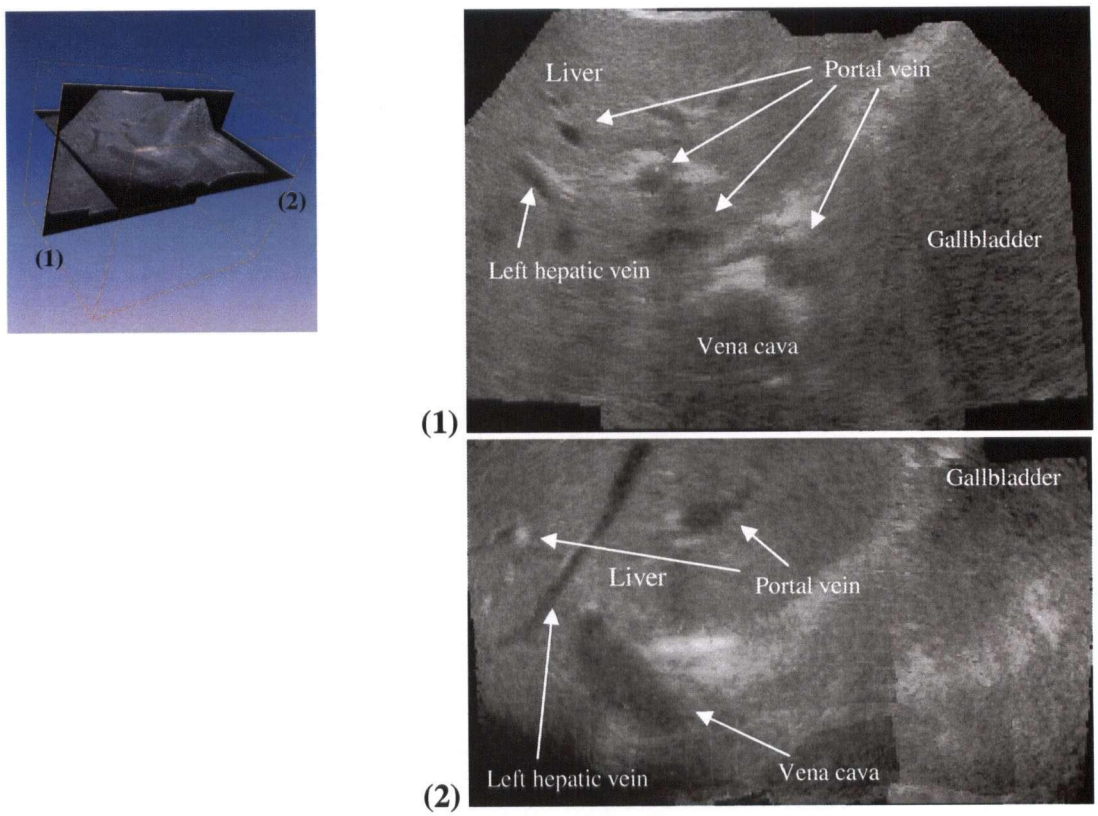

Figure 3 - 5 : Experiments *in vivo*. The locations of the two re-slices of the liver (left). The re-slices reveals the spatial relationship of the structure around the liver (1 & 2). (Block-based warping registration was used.)

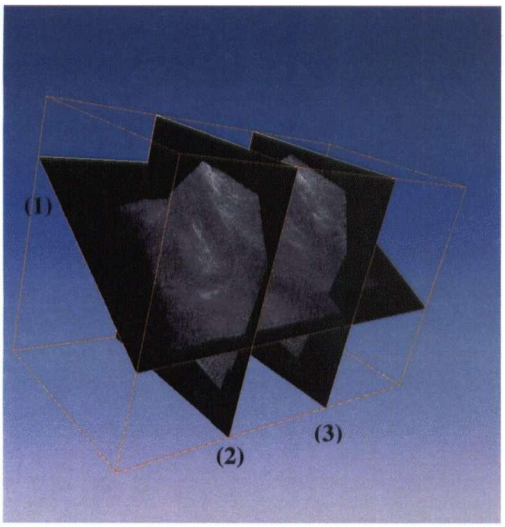

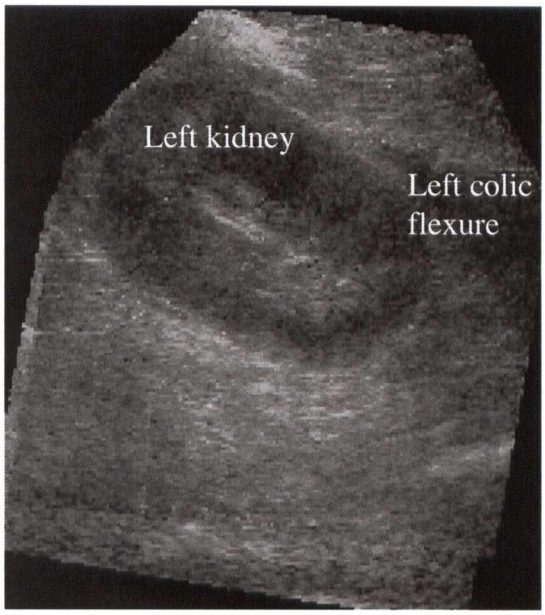

(2)

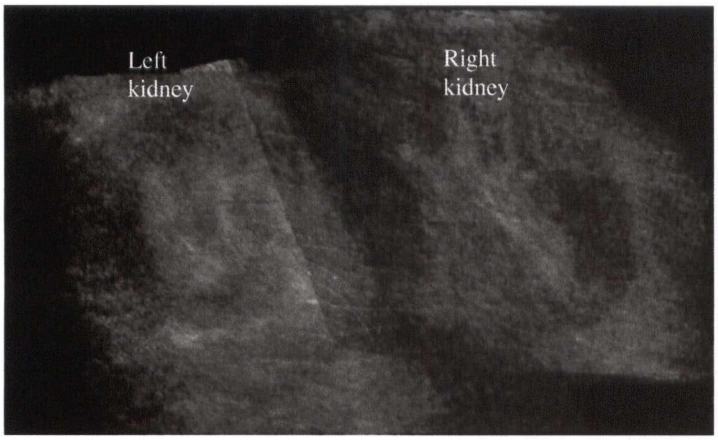

(1)

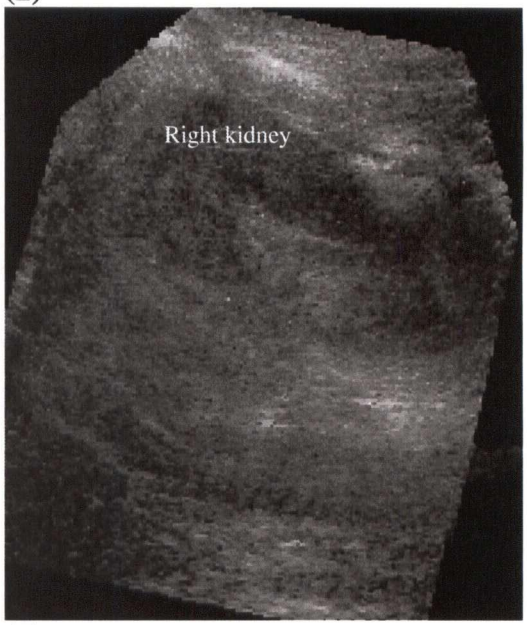

(3)

Figure 3 - 6 : Experiments *in vivo*. The locations of the three re-slices of the kidneys (upper left). The re-slices reveal the spatial relationship of the kidneys (1, 2 & 3). (Block-based warping registration was used.)

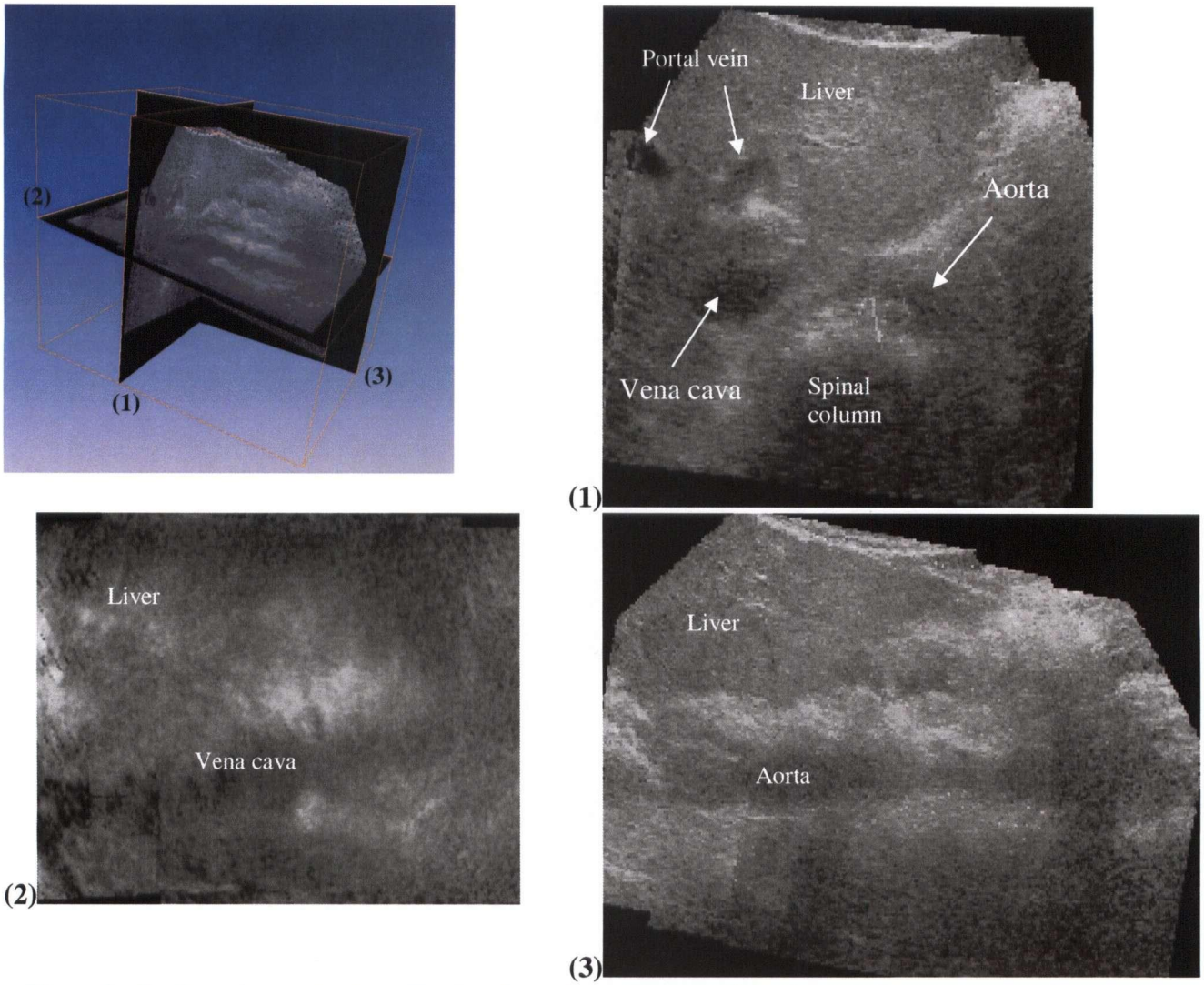

Figure 3 - 7 : Experiments *in vivo*. The locations of the three re-slices of the abdomen (upper left). The three re-slices reveal the spatial relationship of the vessels in the abdomen (1, 2 & 3). (Block-based warping registration was used.)

Tables 3-1 to 3-6 list the results from the reproducibility tests. Ten extended volumes are compared in a pair-wise manner (45 pairs) and the correlation coefficients are calculated as a measure of similarity. For tests *in vitro*, block-based rigid-body registration gives a slightly higher reproducibility than simple compounding (Table 3-1), but block-based warping registration is significantly higher than either one (Tables 3-1 and 3-2). Statistical significance is calculated with the pair-wise student t-test ($\alpha = 0.05$). Similarly for the study *in vivo*, the block-based rigid-body registration is significantly more reproducible than simple compounding (Table 3-4), and block-based warping registration

is significantly more reproducible than block-based rigid-body registration for the tests *in vivo* (Table 3-6).

Table 3 - 1 : Reproducibility of the extended field-of-view volumes. Paired-sample t-test (45 pairs) of *in vitro* (phantom) reproducibility between simple compounding and block-based rigid-body registration.

	Correlation coefficients		
	Simple compounding	**Block-based rigid-body registration**	**Difference**
Mean	0.888	0.890	0.00204
Standard deviation	0.0142	0.00941	0.0151
		Test statistic	0.905
		t(0.05; 44)	1.68

Table 3 - 2 : Reproducibility of the extended field-of-view volumes. Paired-sample t-test (45 pairs) of *in vitro* (phantom) reproducibility between simple compounding and block-based warping registration.

	Correlation coefficients		
	Simple compounding	**Block-based warping registration**	**Difference**
Mean	0.888	0.896	0.00828
Standard deviation	0.0142	0.00994	0.0169
		Test statistic	3.30
		t(0.05; 44)	1.68

Table 3 - 3 : Reproducibility of the extended field-of-view volumes. Paired-sample t-test (45 pairs) of *in vitro* (phantom) reproducibility between block-based rigid-body registration and block-based warping registration.

	Correlation coefficients		
	Block-based rigid-body registration	**Block-based warping registration**	**Difference**
Mean	0.890	0.896	0.00624
Standard deviation	0.00941	0.00983	0.00539
		Test statistic	7.77
		t(0.05; 44)	1.68

Table 3 - 4 : Reproducibility of the extended field-of-view volumes. Paired-sample t-test (45 pairs) of *in vivo* reproducibility between simple compounding and block-based rigid-body registration.

	Correlation coefficients		
	Simple compounding	**Block-based rigid-body registration**	**Difference**
Mean	0.605	0.627	0.0222
Standard deviation	0.0388	0.0353	0.0172
		Test statistic	8.67
		t(0.05; 44)	1.68

Table 3 - 5 : Reproducibility of the extended field-of-view volumes. Paired-sample t-test (45 pairs) of *in vivo* reproducibility between simple compounding and block-based warping registration.

	Correlation coefficients		
	Simple compounding	**Block-based warping registration**	**Difference**
Mean	0.605	0.628	0.0234
Standard deviation	0.0388	0.0364	0.0166
		Test statistic	9.44
		t(0.05; 44)	1.68

Table 3 - 6 : Reproducibility of the extended field-of-view volumes. Paired-sample t-test (45 pairs) of *in vivo* reproducibility between block-based rigid-body registration and block-based warping registration.

	Correlation coefficients		
	Block-based rigid-body registration	**Block-based warping registration**	**Difference**
Mean	0.627	0.628	0.00120
Standard deviation	0.0353	0.0360	0.00241
		Test statistic	3.34
		t(0.05; 44)	1.68

Tables 3-7 to 3-12 list the results of the improvement in registration. Ten extended volumes are compared of the fetus phantom *in vitro* and thirty extended volumes of the abdomen *in vivo*. The two reconstruction methods with block-based registration both aim to increase the correlation coefficient. The correlation coefficient is calculated after interpolation for each of the blocks. For both tests *in vivo* and *in vitro*, the block-based rigid body registration is significantly better aligned after registration (Tables 3-7 and 3-10). This is also true for block-based warping registration (Tables 3-8 and 3-11). Finally, block-based warping registration is significantly better than block-based rigid-body registration (Tables 3-9 and 3-12).

Table 3 - 7 : Improvement in registration. Paired-sample t-test of *in vitro* similarity measure before and after block-based rigid-body registration.

# of *in vitro* extended volumes = 10	**Correlation coefficients**		
	Before	**After**	**Difference**
Mean	0.811	0.823	0.0126
Standard deviation	0.0136	0.0188	0.0131
		Test statistic	3.05
		t(0.05; 9)	1.83

Table 3 - 8 : Improvement in registration. Paired-sample t-test of *in vitro* similarity measure before and after block-based warping registration.

# of *in vitro* extended volumes = 10	Correlation coefficients		
	Before	**After**	**Difference**
Mean	0.811	0.857	0.0451
Standard deviation	0.0170	0.0186	0.0125
		Test statistic	11.4
		t(0.05; 9)	1.83

Table 3 - 9 : Improvement in registration. Paired-sample t-test of *in vitro* similarity measure between the block-based rigid-body registration and the block-based warping registration.

# of *in vitro* extended volumes in each registration method = 10	Correlation coefficients		
	Block-based rigid-body registration	**Block-based warping registration**	**Difference**
Mean	0.823	0.857	0.0331
Standard deviation	0.0188	0.0186	0.0111
		Test statistic	9.42
		t(0.05; 9)	1.83

Table 3 - 10 : Improvement in registration. Paired-sample t-test of *in vivo* similarity measure before and after block-based rigid-body registration.

# of *in vivo* extended volumes = 30	Correlation coefficients		
	Before	**After**	**Difference**
Mean	0.452	0.467	0.0145
Standard deviation	0.112	0.110	0.0203
		Test statistic	3.92
		t(0.05; 29)	1.70

Table 3 - 11 : Improvement in registration. Paired-sample t-test of *in vivo* similarity measure before and after block-based warping registration.

# of *in vivo* extended volumes = 30	Correlation coefficients		
	Before	**After**	**Difference**
Mean	0.453	0.481	0.0286
Standard deviation	0.113	0.115	0.0297
		Test statistic	5.27
		t(0.05; 29)	1.70

Table 3 - 12 : Improvement in registration. Paired-sample t-test of *in vivo* similarity measure between the block-based rigid-body registration and the block-based warping registration.

# of *in vivo* extended volumes in each registration method = 30	Correlation coefficients		
	Block-based rigid-body registration	**Block-based warping registration**	**Difference**
Mean	0.467	0.481	0.0144
Standard deviation	0.110	0.115	0.0132
		Test statistic	5.97
		t(0.05; 29)	1.70

Table 3-13 lists the results of the reconstruction accuracy tests. Figure 3-8 shows a typical measurement. The block-based warping registration produces significantly smaller errors than the two other methods. The block-based rigid-body registration is not significantly different than simple compounding.

(a)

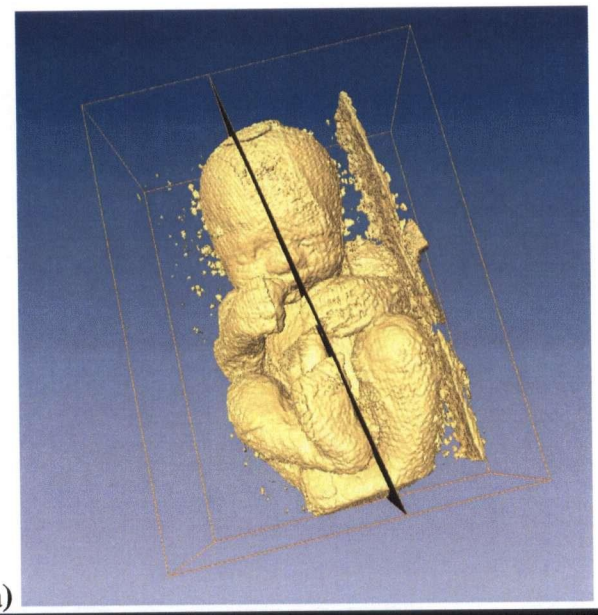

(b)

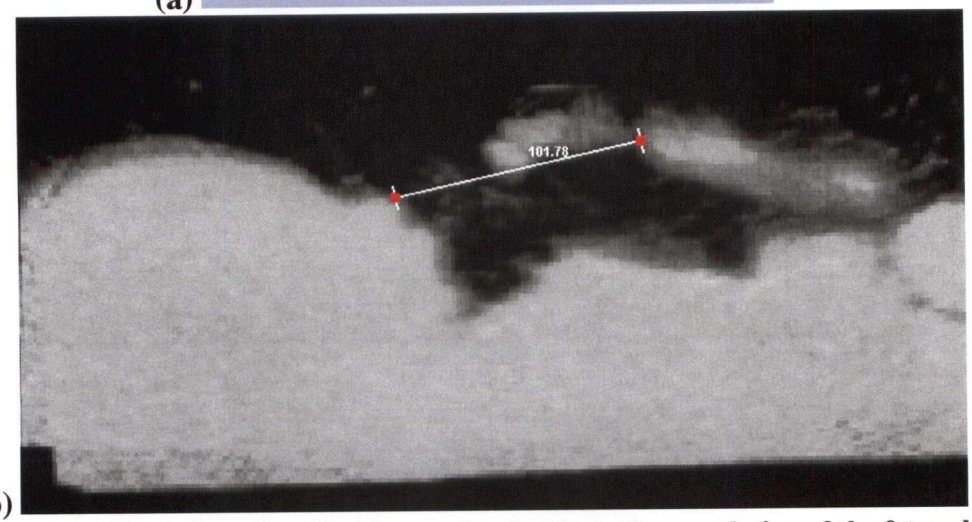

Figure 3 - 8 : Experiments *in vitro*. (a) An example of an isosurface rendering of the fetus phantom and the oblique slice that intersects the two identifiable points (the tip of the nose and the right big toe). (b) The oblique slice used for distance measurement.

Table 3 - 13 : Reconstruction accuracy. This test measures the errors of the distances between two identifiable points in the extended volumes.

	Simple compounding	Block-based rigid-body registration	Block-based warping registration
# of *in vitro* extended volumes	10	10	10
Max error (mm)	4.5	8.0	0.9
RMS error (mm)	2.7	4.0	0.5

3.8 Discussion

Block-based warping registration produced the best results in all tests. This indicates first that there is a need for registration – the position tracker measurements alone are not sufficient. The sources of alignment error are significant and clearly visible in many of the examinations. The use of warping also produced significantly better results than rigid-body registration of the blocks. This indicates that interpolation of the control points, even with simple linear interpolation, is needed for a good match of the features. Even though the blocks are small, interpolation within the block is needed to correct for distortions.

Using block-based warping registration on the examinations of the abdomen produced visibly good results. The quality of the reslices was generally similar to the quality of the individual volumes. Little quality appears to have been lost during reconstruction of the extended field of view. Such extended field of view examinations may therefore eventually find utility in clinical applications. For example diagnostics and surgical planning may benefit from the depiction of large organs in a single view or the path of a tool towards a target.

Yet some issues of image quality remain. Some reslice directions produces somewhat poorer quality images than other directions. Figure 3-6 is an example. This appears to be related to the quality of the individual volumes. Despite the dedicated nature of the 3D Voluson probe, the quality in the elevation direction is still slightly poorer than the lateral direction and affects the extended field of view. Other probes, such as a phased array 3D probe, may produce more consistent image quality in all directions.

A phased array 3D probe also has a much faster acquisition rate than the current swept-array probe. With a faster probe, the hold-and-shoot protocol could be replaced with continuous acquisition in the same manner as current 2D panorama systems. The overlap among volumes would be even larger and the registration ranges would likely be smaller. This may reduce the registration errors that need to be corrected. Such a probe may also produce higher image quality in the elevation direction.

The speed of reconstruction remains a significant issue. Simple compounding takes only two minutes to reconstruct the extended field of view for a typical acquisition of six volumes. Block-based rigid-body registration takes 33 minutes and block-based

warping registration takes 40 minutes. These reconstruction times are too long for clinical acceptance. The major computational task is the registration of the blocks but interpolation still adds a significant amount of time. The computations were performed on a state-of-the-art 64-bit workstation, so it is unlikely that advances in workstation processors will solve this problem in the near future. Modern ultrasound machines with 2D extended field of view solve the problem using dedicated digital signal processing chips and specialized circuit boards. 3D extended field of view will likely need to follow a similar approach to produce acceptable reconstruction times.

Compared to freehand 3D ultrasound, volume-based extended field of view is slightly easier to operate. In freehand 3D ultrasound, the sonographer needs to carefully sweep the probe over the region while maintaining good alignment and velocity of the probe so that the stack of images does not contain any gaps. The image quality in freehand 3D ultrasound is also affected by the direction of the sweep, especially the orientation of the elevation direction. Clinical trials on a variety of applications need to be performed with the proposed 3D extended field of view system to gain a better understanding of the potential advantages, including ease-of-use.

3.9 Conclusion

In this study, three methods were demonstrated to automatically reconstruct an extended field of view from a set of 3D ultrasound volumes. The key was the alignment of the overlapping regions. A block-based warping registration was necessary to correct the errors of alignment. The warping method improved the reproducibility of the reconstructed volumes so that the anatomy was constructed the same way each time it is examined. The warping method significantly improved alignment by subdividing the overlapping regions into a set of blocks, and searching for the position and orientation with the maximum correlation coefficient. The geometric accuracy of the extended volumes with a 4-8 MHz probe created by block-based warping registration is measured by point-to-point distance accuracy of less than a millimeter.

Although the quality of the extended field of view images appears good, the main practical issue remains reconstruction time. Implementation on a general-purpose

workstation produces reconstruction times of approximately 40 minutes. Implementation on dedicated hardware is needed for clinically acceptable speeds.

Chapter 4 Conclusions and Future Directions

Medical imaging is a representation of the reality inside the human body. Ultrasound is a safe and noninvasive modality that is useful for diagnosis. This thesis explored the use of a position sensor for volume tracking and applied the volume tracking technique for extended field-of-view applications.

4.1 Probe Calibration

Probe calibration is a necessary step to reveal the spatial position of an anatomical structure. This spatial information is needed in several applications including image-guided surgery and radiation therapy. The study developed three different calibration methods and derived a mathematical model for each method. All methods have the same purpose, that is to compute the transformation matrix between the volume and the probe coordinate systems. A series of tests were established to evaluate the results of different methods, namely calibration reproducibility, point accuracy and reconstruction accuracy by distance measure.

The tests showed that the IXI-wire method has the best overall performance among the three. The advantage of this method is its high accuracy in point and distance measures. Also, a reference volume produced from the stylus measurement can be used multiple times and this saves time and effort for repeat calibrations.

4.2 Extended Field-of-View

2D extended field-of-view has established its acceptability in clinical diagnostics. The new generation of the 3D probe and the use of the volume-tracking system make volume extended field-of-view possible. The study developed the registration system that takes multiple individual volumes with their spatial information (positions and orientation) to produce an extended volume. Three registration methods, namely simple compounding, block-based rigid-body registration and block-based warping registration, are compared in different aspects to determine the most accurate method. The tests include

reconstruction reproducibility, improvement over similarity and reconstruction accuracy by distance measure.

According to the test results, the block-based warping registration is desirable to model the matching among overlapping ultrasound volumes that are subject to various artifacts. The *in vivo* experiments proved that the concept of volume extended field-of-view is feasible for clinical applications.

4.3 Future Directions

There are areas for further developments related to the two technologies presented in this thesis.

4.3.1 Fast Calibration by Beam Shadowing

The calibration methods described in Chapter 2 require volume imaging of phantoms with known geometrical properties with respect to a fixed coordinate system. The geometrical properties are obtained by the use of the stylus. In the IXI-wire method, the wires' positions must be measured for the reconstruction of a reference volume. In the cube method, the three flat surfaces of the cube must be measured for the calculations of the corresponding plane equations. In the stylus method, the stylus must be calibrated to find the vector to its tip. These time-consuming procedures are the mandatory for the computation of the calibration solution.

Calibration by beam shadowing is a novel idea to accomplish fast calibration. It does not require a phantom but needs an apparatus attached on the probe to block a small portion of ultrasound beam. The apparatus rigidly holds a few beads touching the surface of the probe head and the sphere-shape beads should not damage the sensitive surface. The calibration procedure first uses the stylus to measure the positions of the beads with respect to the probe (P) coordinate system. Any volume acquired from the probe will contain bead shadows that originate in the beads with known positions (Figure 4-1). The matching of the bead shadows in volume coordinates with their positions in the probe

coordinates provide a mathematical model for finding the transformation solution, ${}^{V}\mathbf{T}_{P}$, between the probe (P) and the volume (V) coordinate systems.

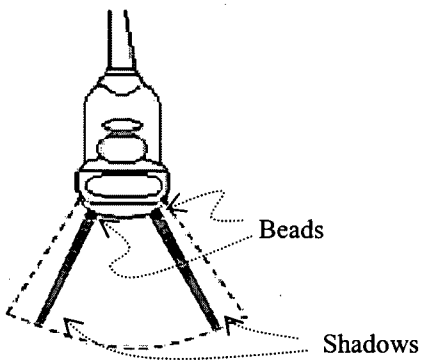

Figure 4 - 1 : An image plane in the volume contains shadows because the ultrasound beam is partially blocked by beads.

The advantage of this method is to provide a rapid calibration solution without the need of a phantom. Every single volume acquired from the probe can be used for calibration. The shadow features are desirable for robust operation because they are clearly identifiable. Since the shadow region only occupies a small portion of the ultrasound volume, the same volume for anatomical imaging can also be used for calibration. This is practically useful for sonographers who frequently modify the size of volume on the ultrasound scanner during the examination. This is because the calibration solution varies according to the size of volume. Without this method, a substantial amount of effort and time is needed to calculate the calibration solutions for all possible sizes that are used during the examination. Therefore, the volume that contains both the anatomical information and the calibration features saves a tremendous amount of time in volume tracking because only the applicable sizes require calibration solutions. This system should be developed, tested and compared with other calibration methods.

4.3.2 Spatial Compounding

Spatial compounding averages multiple overlapping data (image or volume) for the purpose of reducing speckle. The speckle pattern at a particular region changes when the beam angle is altered. The reason is that the scattering and distribution of ultrasound

echoes changes with the beam path, but the ability to detect strong anatomical structures remains the same. This suggests that spatial compounding over the same anatomical structure is an appropriate method to reduce speckle. Multiple volumes across the same region are acquired in different beam angles and they are first aligned properly by registration before averaging.

The advantages of spatial compounding have been demonstrated by other researchers. It increases the signal-to-noise ratio and improves the visualization to detect anatomical structures. Most of the previous investigations were based on the use of a 2D ultrasound scanner. Even though they applied it on 3D ultrasound, the 3D data set are reconstructed from 2D images and suffer low resolution in the elevational direction. Appendix E gives a survey of the literature, grouped into the two types as mentioned above.

This thesis describes the use of a new generation of 3D probe. Spatial compounding with the 3D probe is the next logical step. The study of extended field-of-view registers partially overlapping volumes to produce extended volumes. The same system can be used for spatial compounding because the concept to produce a compounded volume is almost identical. Spatial compounding registers multiple volumes that are almost fully overlapped because the objective is to reduce speckle by averaging. The same anatomical structure from multiple volumes must be aligned by registration before averaging, to prevent blurring in the final volume. This suggests that the study of spatial compounding can employ the use of the extended field-of-view system and it only requires a new set of tests to evaluate different aspects of the result, such as signal-to-noise ratios (SNR) and volume resolution.

Bibliography

Baba K, Kobayashi K, Hayashi M, et al. Extended field-of-view ultrasound imaging in obstetrics and gynecology: preliminary experience. Ultrasound Obstet Gynecol. 2000 Feb;15(2):157-159.

Barbe C, Troccaz J, Mazier B, Lavallée S.. Using 2.5D echography in computer assisted spine surgery. Proceedings of the 15th Annual International Conference IEEE Engineering in Medicine and Biology Society. Proc IEEE 1993; 160-161.

Beissert M, Jenett M, Wetzler T, et al. Enlarged lymph nodes of the neck: evaluation with parallel extended field-of-view sonographic sequences. J Ultrasound Med. 2000 Mar;19(3):195-200.

Bilaniuk N, Wong GSK. Speed of sound in pure water as a function of temperature. J. Acoust. Soc. Am. 1993; 93(3):1609-1612.

Bouchet LG, Meeks SL, Goodchild G, et al. Calibration of three-dimensional ultrasound images for image-guided radiation therapy. Phys Med Biol 2001;46:559-577.

Canny J. A computational approach to edge detection. IEEE Transactions on Pattern Analysis and Machine Intelligence 1986; 8(6):679-698.

Comeau RM, Fenster A, Peters TM. Integrated MR and ultrasound imaging for improved image guidance in neurosurgery. SPIE 1998 Proceedings, San Diego, USA, 1998;3338:747-754.

Comeau RM, Sadikot AF, Fenster A, Peters TM. Intraoperative ultrasound for guidance and tissue shift correction in image-guided neurosurgery. Med Phys 2000; 27(4):787-800.

Dantas RG, Leeman S, Costa ET, Healey A. Speckle reduction technique in B-mod ultrasound images. Medical Application of Signal Processing 2002;10:1-6.

Detmer PR, Bashein G, Hodges T, et al. 3d ultrasound image feature localization based on magnetic scanhead tracking: *In vitro* calibration and validation. Ultrasound Med Biol 1994; 20(9):923-936.

Dietrich CF, Ignee A, Gebel M, Braden B, Schuessler G. Imaging of Abdomen. Z Gastroenterol. 2002 Dec; 40(12):965-970.

Donald I, MacVicar J, Brown TG. Investigation of abdominal masses by pulsed ultrasound. Lancet 1958; 1:1188-1195.

Edwards WS. A low-cost high-performance three-dimensional ultrasound system and its clinical application in obstetrics. PhD thesis, University of Washington, WA, USA. 1999.

Edwards WS, Deforge C, Kim Y. Interactive three-dimensional ultrasound using a programmable multimedia processor. International Journal of Imaging Systems and Technology. 1998;9(6):442-454.

Evans AN, Nixon MS. Temporal speckle reduction for feature extraction in ultrasound images. Proceedings of Compouter Analysis of Images and Patterns 1993;65-73.

Forsberg F. Ultasonic biomedical technology; marketing versus clinical reality. Ultrasonics. 2004 Apr;42(1-9):17-27.

Forsyth DA, Ponce J. Computer vision -- a modern approach. Upper Saddle River, NJ, USA: Prentice-Hall, 2003.

Gonzalez RC, Woods RE. Digital image processing, 2nd Edition. Upper Saddle River, NJ, USA: Prentice-Hall, 2002.

Groves AR, Rohling RN. Two-dimensional spatial compounding with warping. Ultrasound Med Biol 2004;30(7):929-942.

Guo, D. Speckle reduction of ultrasound images. Proc IEEE, First Joint BMES/EMBS Conference 1999;2:1052.

Henrich W, Fuchs I, Schmider A, Buhling KJ, Dudenhausen JW. Transvaginal and transabdominal extended field-of-view (EFOV) and power Doppler EFOV sonography in gynecology: advantages and applications. J Ultrasound Med. 2002a Oct;21(10):1137-1144.

Henrich W, Fuchs I, Ehrenstein T, et al. Antenatal diagnosis of placenta percreta with planned in situ retention and methotrexate therapy in a woman infected with HIV. Ultrasound Obstet Gynecol. 2002 Jul;20(1):90-93.

Henrich W, Schmider A, Kjos S, Tutschek B, Dudenhausen JW. Advantages of and applications for extended field-of-view ultrasound in obstetrics. Arch Gynecol Obstet. 2003 Jun;268(2):121-127.

Hill CR, Bamber J, ter Haar GR. Physical principles of medical ultrasonics. Chichester, UK; John Wiley & Sons, 2004.

Jespersen SK, Wilhjelm JE, Silesen H. Ultrasound spatial compound scanner for improved visualization in vascular imaging. Proceedings of IEEE Ultrasonics Symposium 1998;2;1623-1626.

Kim SH, Choi BI, Kim KW, Lee KH, Han JK. Extended field-of-view sonography: advantages in abdominal applications. J Ultrasound Med. 2003 Apr;22(4):385-394.

Kremkau FW. Diagnostic Ultrasound: Principles and instruments, 6th Edition. Philadelphia, PA, USA: W.B. Saunders, 2002.

Krücker JF, LeCarpentier GL, Fowlkes JB, Carson PL. Rapid elastic image registration for 3D ultrasound. IEEE Trans Med Imag 2002;11:1384-1394.

Krücker JF, Meyer CR, LeCarpentier GL, Fowlkes JB, Carson PL. 3D spatial compounding of ultrasound images using image based nonrigid registration. Ultrasound Med Biol. 2000;26;1475-1488.

Lacefield JC, Pilkington WC, Waag RC. Comparisons of lesion detectability in ultrasound images acquired using time-shift compensation and spatial compounding. IEEE Transactions on Ultrasonics, Ferroelectrics, and Frequency Control 2004;51;12;1679-1659.

Lange T, Eulenstein S. Calibration of swept-volume 3D ultrasound. Proceedings of Medical Image Understanding and Analysis, Portsmouth, UK, July 22-23, 2002; 3: Calibration and Motion.

Leotta, DF, Martin RW. Three-dimensional spatial compounding of ultrasound scans with weighting by incidence angle. Ultrasonic Imaging 2000a;22;1-19.

Leotta, DF, Martin RW. Three-dimensional ultrasound imaging of the rotator cuff: spatial compounding and tendon thickness measurement. Ultrasonic Imaging 2000b;26;509-525.

Leung YL, Roshier AL, Johnson S, Kerslake R, McNally DS. Demonstration of the appearance of the paraspinal musculoligamentous structures of the cervical spine using ultrasound. Clin Anat. 2005 Mar;18(2):96-103.

Lin EC, Middleton WD, Teefey SA. Extended field of view sonography in musculoskeletal imaging. J Ultrasound Med. 1999 Feb;18(2):147-152.

Lindseth F, Tangen G, Langø T, Bang J. Probe calibration for freehand 3D ultrasound. Ultrasound Med Biol 2003; 29(11)1607-23.

Loizou C, Christodoulou C, Pattichis CS, et al. Speckle reduction in ultrasound images of atherosclerotic carotid plaque. International Conference on Digital Signal Processing 2002; 2:525-528.

Mathwes JH, Fink KK. Numerical methods using Matlab, 4th Edition. Upper Saddle River, NJ, USA: Prentice-Hall, 2004.

Mercier L, Langø T. Lindseth F, Collins L. A review of calibration techniques for freehand 3D ultrasound systems. Ultrasound Med Biol 2005; 31(2): 143-165.

Muratore DM, Galloway LJ. Beam calibration without a phantom for creating a 3D ultrasound system. Ultrasound Med Biol 2001; 27:1557-1566.

Nelson TR, Elvins TT. Visualization of 3D ultrasound data. IEEE Computer Graphic and Applications 1993; 13(6):50-57.

Ourselin S, Roche A, Prima S, Ayache N. Block matching: a general framework to improve robustness of rigid registration of medical images. MICCAI 2000. Pittsburgh, USA, Springer, Lecture Notes in Computer Science, 2000;557-566.

Pagoulatos N, Haynor DR, Kim Y. Fast calibration for 3D ultrasound imaging and multimodality image. Proc IEEE, First Joint BMES/EMBS Conference (Serving Humanity, Advancing Technology), Atlanta, GA, USA, 1999:1065.

Pagoulatos N, Haynor DR, Kim Y. A fast calibration method for 3D tracking of ultrasound images using a spatial localizer. Ultrasound Med Biol 2001; 27:1219-1229.

Pagoulatos N, Haynor DR, Kim Y. Intensity-based image registration for 3D spatial compounding using a freehand 3D ultrasound system. SPIE Proc 2002;4687:438-449.

Parent R. Computer animation: Algorithms and techniques. San Francisco, CA, USA: Morgan Kaufmann, 2002.

Peetrons P. Ultrasound of muscles. Eur Radiol. 2002 Jan;12(1):35-43.

Poon TC, Rohling RN. Comparison of calibration methods for spatial tracking of a 3D ultrasound probe. Ultrasound Med Biol. 2005 (in press).

Powell MJD. A Fortran subroutine for solving systems of nonlinear algebraic equations. Numerical Methods for Nonlinear Algebraic Equations (P. Rabinowitz, ed.) 1970; 7.

Prager RW, Rohling RN, Gee AH, Berman L. Rapid calibration for 3D freehand ultrasound. Ultrasound Med Biol 1998; 24:855-869.

Press WH, Teukolsky SA, Vetterling WT, Flannery BP. Numerical Recipes in C, 2nd Edition. Cambridge, UK: Cambridge University Press, 1992.

Riccabona M. Potential of modern sonographic techniques in paediatric uroradiology. Eur J Radiol. 2002 Aug;43(2):110-121.

Rohling RN. 3D freehand ultrasound: reconstruction and spatial compounding. Ph.D thesis, University of Cambridge, UK. 1998.

Rohling RN, Gee AH. Correcting motion-induced registration errors in 3D ultrasound images. Proc. of the British Machine Vision Conference. Edinburgh, UK, 1996;645-654.

Rohling RN, Gee AH, Berman L. Automatic registration of 3D ultrasound images. Ultrasound Med Biol. 1998 Jul;24(6):841-854.

Rohling RN, Gee AH, Berman L. 3D spatial compounding of ultrasound images. Med Image Anal 1997;1:177-193.

Rohling RN, Munger P, Hollerbach JM, Peters T. Comparison of relative accuracy between a mechanical and an optical position tracker for image-guided neurosurgery. Journal of Image Guided Surgery 1995; 1(1):30-34.

Sauerbrei EE. Extended field-of-view sonography: utility in clinical practice. J Ultrasound Med. 1999 May;18(5):335-341.

Sciavicco L, Siciliano B. Modelling and control of robot manipulators. Springer-Verlag London Limited, 1996.

Shanker PM. Speckle reduction in ultrasound B-scans using weighted averaging in spatial compounding. IEEE Transactions on Ultrasonics, Ferroelectrics and Frequency Control 1986;6;754-758.

Sofka CM, Adler RS. Sonographic evaluation of shoulder arthroplasty. AJR Am J Roentgenol. 2003 Apr;180(4):1117-1120.

Techavipoo U, Chen Q, Varghese T, Zagzebski JA, Madsen EL. Spatial angular compounding for ultrasound elastography. Proceedings of the 2nd IEEE International Symposium on Biomedical Imaging. Proc IEEE 2004;1;1;972-975.

Tirumalai A, Weng L, Grassmann A, et al. New ultrasound image display with extended field of view. SPIE Proc 1997; 3031:409-419.

Trahey GE, Smith SW, von Ramm OT. Speckle reduction in medical ultrasound via spatial compounding. SPIE 1986 Proceedings, San Diego, USA, 1998;626:290-300.

Trobaugh JW, Trobaugh DJ, Richard WD. Three-dimensional imaging with stereotactic ultrasonography. Comput Med Imaging Graph 1994; 18(5):315-323.

Wells PNT. Current Status and Future Technical Advances of Ultrasonic Imaging. IEEE Engineering in Medicine and Biology 2000;19(5):14-20.

Wells PNT. Ultrasonic imaging of the human body. Rep Prog Phys 1999;62:671-722.

WFUMB. World Federation for Ultrasound in Medicine and Biology News. Ultrasound Med Biol 1997; 23:974.

Woydt M, Vince GH, Krauss J, et al. New ultrasound techniques and their application in neurosurgical intra-operative sonography. Neurol Res. 2001 Oct;23(7):697-705.

Xue K, He P, Wang Y. A motion compensated ultrasound spatial compounding algorithm. Proceedings of the 19th Annual International Conference IEEE Engineering in Medicine and Biology Society. Proc IEEE 1997; 818-821.

Ying M, Sin MH. Comparison of extended field of view and dual image ultrasound techniques: accuracy and reliability of distance measurements in phantom study. Ultrasound Med Biol. 2005 Jan;31(1):79:83.

Appendix A Rigid Body Transformations

Rigid body transformations are defined as geometrical transformations that preserve all distances and scales of the body itself. Each volume that is involved in a registration will be referred to a coordinate system, which defines a space for that volume. It is described as a rigid body in space by its position and orientation with respect to a reference frame (Sciavicco and Siciliano, 2004). Figure A-1 illustrates a typical rigid body transformation of a volume.

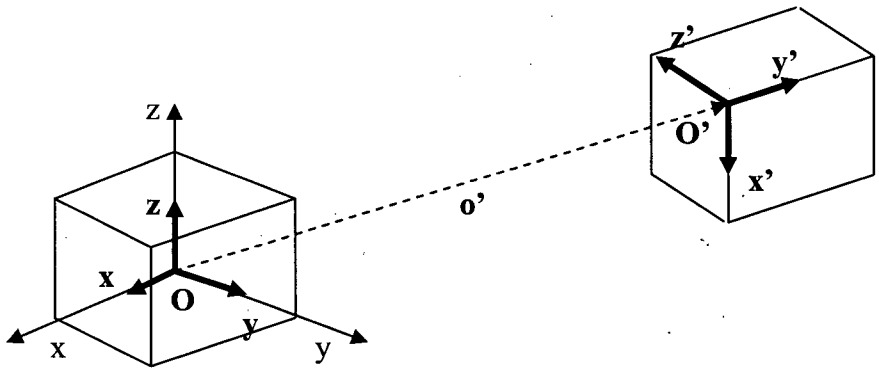

Figure A – 1 Position and orientation of a Rigid Body

Let *O-xyz* be the orthonormal reference frame. The position of the origin *O'* on the transformed rigid body with respect to the reference frame is expressed by the relation:

$$\boldsymbol{O'} = o'_x \boldsymbol{x} + o'_y \boldsymbol{y} + o'_z \boldsymbol{z}, \tag{A-1}$$

where $\boldsymbol{o'}$ denotes the vector from the origin of the reference frame to the origin of the transformed frame to describe the translation. The transformed frame, *O'-x'y'z'* can also be expressed with respect to the reference frame *O-xyz* by the following equations:

$$\boldsymbol{x'} = x'_x \boldsymbol{x} + x'_y \boldsymbol{y} + x'_z \boldsymbol{z} \tag{A-2}$$

$$\boldsymbol{y'} = y'_x \boldsymbol{x} + y'_y \boldsymbol{y} + y'_z \boldsymbol{z} \tag{A-3}$$

$$\boldsymbol{z'} = z'_x \boldsymbol{x} + z'_y \boldsymbol{y} + z'_z \boldsymbol{z} \tag{A-4}$$

Vectors $\boldsymbol{x'}$, $\boldsymbol{y'}$ and $\boldsymbol{z'}$ are orthonormal unit vectors to specify the orientation of the transformed frame with respect to the reference frame. Let *p* be a point in the reference frame. To transform *p* in *O-xyz* to *p'*, it can be expressed by the relation:

$$\boldsymbol{P'} = \mathbf{R}\,\boldsymbol{p} + \mathbf{o'} \tag{A-5}$$

where **R** is the rotation matrix to transform from $[x\ y\ z]^T$ to $[x'\ y'\ z']^T$. **R** is a 3x3 orthogonal matrix, meaning that $\mathbf{R}^T\mathbf{R} = \mathbf{R}\mathbf{R}^T = \mathbf{I}$.

A-1 Rotation Matrix

Any rotation can be characterized in terms of three angles of rotation, α, β, γ, about the respective Cartesian axes. Suppose that the reference frame *O-xyz* is rotated by an angle α about the *z*-axis to form *O'-x'y'z'*. The rotation matrix of *O'-x'y'z'* with respect to *O-xyz* is:

$$\mathbf{R}_z(\alpha) = \begin{bmatrix} \cos\alpha & -\sin\alpha & 0 \\ \sin\alpha & \cos\alpha & 0 \\ 0 & 0 & 1 \end{bmatrix} \tag{A-6}$$

It can also be shown that the rotations by an angle β about the *y*-axis and by an angle γ about the *x* –axis are respectively given by:

$$\mathbf{R}_y(\beta) = \begin{bmatrix} \cos\beta & 0 & \sin\beta \\ 0 & 1 & 0 \\ -\sin\beta & 0 & \cos\beta \end{bmatrix} \tag{A-7}$$

$$\mathbf{R}_x(\gamma) = \begin{bmatrix} 1 & 0 & 0 \\ 0 & \cos\gamma & -\sin\gamma \\ 0 & \sin\gamma & \cos\gamma \end{bmatrix} \tag{A-8}$$

Thus, the rotation of a volume about the ***x***, ***y***, and *z* axes, in that order leads to:

$$\mathbf{R}\,(\alpha, \beta, \gamma) = \mathbf{R}_x(\alpha)\,\mathbf{R}_y(\beta)\,\mathbf{R}_x(\gamma) \tag{A-9}$$

$$\mathbf{R}(\alpha,\beta,\gamma) = \begin{bmatrix} \cos\beta\cos\gamma & -\cos\alpha\sin\gamma + \sin\alpha\sin\beta\cos\gamma & \sin\alpha\sin\gamma + \cos\alpha\sin\beta\cos\gamma \\ \cos\beta\sin\gamma & \cos\alpha\cos\gamma + \sin\alpha\sin\beta\sin\gamma & -\sin\alpha\cos\gamma + \cos\alpha\sin\beta\sin\gamma \\ -\sin\beta & \sin\alpha\cos\beta & \cos\alpha\cos\beta \end{bmatrix}$$

(A-10)

The matrix (A-10) will be useful to describe rotations about an arbitrary axis in space.

A-2 Homogeneous Transformations of Volumes

As described at the beginning of this section, each volume is considered as a rigid body. The position of a volume in space is expressed in terms of translations and rotations with respect to the reference frame. The transformation of an arbitrary point p in the reference frame is expressed as:

$$\boldsymbol{p'} = \mathbf{R}\,\boldsymbol{p} + \mathbf{o'} \tag{A-11}$$

Eqn. (A-11) above represents the coordinate transformation of an arbitrary point between two frames. To achieve a compact representation of the transformation, the homogeneous transformation matrix is used and is expressed as:

$$\mathbb{P}' = \mathbf{A}\,\mathbb{P} \tag{A-12}$$

where $\mathbb{P} = [\,\boldsymbol{p}\ 1\,]^{\mathrm{T}}$ and $A = \begin{bmatrix} R & \mathbf{o'} \\ 0^T & 1 \end{bmatrix}$. The transformed coordinate is expressed as $\mathbb{P}'$ $= [\,\boldsymbol{p'}\ 1\,]^{\mathrm{T}}$.

Appendix B Correlation Coefficient in Block-Based Registration

The correlation function used as a similarity measure is the normalized cross-correlation. The coefficient, $c(x, y, z)$ (eqn. B-1), is scaled (normalized) in the range -1.0 to 1.0, providing a uniform scale (Gonzalez and Woods 2002). The value of $c(x, y, z)$, calculating the correlation function between V_{ref} and the overlapping block of V_{adj}, is

$$c(x, y, z) = \frac{\sum_s \sum_t \sum_u [V_{ref}(s,t,u) - \overline{V_{ref}}(s,t,u)][V_{adj}(x+s, y+t, z+u) - \overline{V_{adj}}]}{\sqrt{\sum_s \sum_t \sum_u [V_{ref}(s,t,u) - \overline{V_{ref}}(s,t,u)]^2 \sum_s \sum_t \sum_u [V_{adj}(x+s, y+t, z+u) - \overline{V_{adj}}]^2}} \quad \text{(B-1)}$$

where $\overline{V_{ref}}$ and $\overline{V_{adj}}$ are the average value of V_{ref} and V_{adj}, respectively, in the common overlapping region and the summations are calculated over the region only. Although the orientation parameters, (α, β, γ), are not shown in the eqn (B-1), they are still the variables of the equation. The orientation of any V_{adj} is applied with respect to the coordinate system of V_{ref} before the calculation of the correlation coefficient.

Appendix C Linear Interpolation with Control Points

After the registrations of all the blocks (the composition of V_{adj}) to V_{ref}, the transformation result of each block is designated to the center voxel (control point) of the block. The rest of the voxels in the block are then interpolated linearly. This is a 3D interpolation procedure accomplished by a sequence of 1-D interpolations. The lines of unknown voxels that are located on the same rows with the control points are interpolated first. Then, these lines of voxels with known transformation values are then used to interpolate planes intersecting with them. Finally, those planes of voxels with known transformation values are used to fill the rest of the voxels in the V_{adj}. The equation of the linear interpolation to find the unknown transformation parameter, y, at the voxel position, x is:

$$y = \frac{x_{j+1} - x}{x_{j+1} - x_j} y_j + \frac{x - x_j}{x_{j+1} - x_j} y_{j+1} \qquad \text{(C-1)}$$

where x_j and y_j are the position and the transformation parameter, respectively, of the control point or the known point (voxel) by previous interpolations, with j equal to the index of known (or control) point in a row. For every voxel, there are six transformation parameters (x, y, z, α, β, γ) to specify its spatial position. This implies that the above equation is applied six times for each parameter on one unknown point (voxel).

Appendix D Powell's method

The goal of registration is to search for the maximum of the correlation coefficient function f_C over the six spatial variables (three positions and three orientation angles). Powell's method is used for this search. It initializes a set of the spatial variables as standard base vectors, $\mathbf{U}_k = \boldsymbol{e}_k$ (for $k = 1...6$). Denote $\mathbf{X}_0$ as the position measurement of V_{adj} overlapping with V_{ref}. Powell's method finds the next position $\mathbf{X}_1$, which is the next maximum of f_C, by traveling successively along each of the six standard base vectors, $\mathbf{U}_k$. It repeats in a number of iterative steps i (> 0) until the ultimate maximum $\mathbf{X}$, is found. In each step, $\mathbf{U}_k$ is modified to a set of direction vectors that are likely to reach a further extreme. The algorithm of minimization (or maximization when $f = -f_C$) is summarized in the following steps (Mathews and Fink 2004):

1. Set the initial position (Optotrak measurement) of the block equal to $\mathbf{X}_i$, where i equals zero here.
2. Set $\mathbf{P}_0 = \mathbf{X}_i$, where $\mathbf{P}_k$ is the variable in f such that the minimization of $f(\mathbf{P}_k)$ along one vector direction is a single-variable problem.
3. For $k = 1, 2, ..., 6$ find the value of γ_k that minimizes $f(\mathbf{P}_{k-1} + \gamma_k\mathbf{U}_k)$ and set $\mathbf{P}_k = \mathbf{P}_{k-1} + \gamma_k\mathbf{U}_k$, where f is a minimum from the successive minimization along each $\mathbf{U}_k$ direction.
4. Set r and $\mathbf{U}_r$ equal to the maximum decrease in f and the direction of the maximum decrease, respectively, over all the direction vectors in step (3).
5. Increment $i = i + 1$.
6. If $f(2\mathbf{P}_N - \mathbf{P}_0) \geq f(\mathbf{P}_0)$
   or $2[f(\mathbf{P}_0) - 2f(\mathbf{P}_N) + f(2\mathbf{P}_N - \mathbf{P}_0)][f(\mathbf{P}_0) - f(\mathbf{P}_N) - r]^2 \geq r[f(\mathbf{P}_0) - f(2\mathbf{P}_N - \mathbf{P}_0)]^2$,
   then set $\mathbf{X}_i = \mathbf{P}_N$ and return to step (2). Otherwise, go to step (7).
7. Set $\mathbf{U}_r = \mathbf{P}_N - \mathbf{P}_0$.
8. Find the value of γ that minimizes $f(\mathbf{P}_0 + \gamma\mathbf{U}_r)$. Set $\mathbf{X}_i = \mathbf{P}_0 + \gamma\mathbf{U}_r$.
9. Repeat steps (2) through (8) until $\| \mathbf{X}_i - \mathbf{X}_{i-1} \|$ is smaller than a threshold value.

The two conditions in step (6) determine whether it is necessary to search for a further decrease in the $\mathbf{P}_N - \mathbf{P}_0$ direction.

Appendix E Literature Review on Spatial Compounding

Table E - 1 : Examples from the literatures on spatial compounding.

Type of data set	Author(s)	Journal title (The sources of the journals are listed in the Bibliography section.)
2D images	Shankar 1986.	Speckle reduction in ultrasound B-scans using weighted averaging in spatial compounding.
	Trahey et al. 1986.	Speckle reduction in medical ultrasound via spatial compounding.
	Lacefield et al. 2004.	Comparisons of lesion detectability in ultrasound acquired using time-shift compensation and spatial compounding.
	Groves and Rohling 2004.	Two-dimensional spatial compounding with warping
	Techavipoo et al. 2004.	Spatial angular compounding for ultrasound elastrography.
3D data set reconstructed by 2D images	Rohling et al. 1997.	3D Spatial Compounding of ultrasound images.
	Xue et al. 1997.	A motion compensated ultrasound spatial compounding algorithm.
	Jespersen et al. 1998.	Ultrasound spatial compound scanner for improved visualization in vascular imaging.
	Krücker et al. 2000.	3D spatial compounding of ultrasound images using image-based nonrigid registration.
	Leotta and Martin 2000a.	Three-dimensional spatial compounding of ultrasound scans with incidence angle weighting.
	Leotta and Martin 2000b.	Three-dimensional ultrasound imaging of the rotator cuff: spatial compounding and tendon thickness measurement.
	Pagoulatos et al. 2002.	Intensity-based image registration for 3D spatial compounding using a freehand 3D ultrasound system.